

MASTER

Determination of the passive transverse mechanical properties of skeletal muscle under in vivo compression

Braakman, Niels

Award date:
2003

[Link to publication](#)

Disclaimer

This document contains a student thesis (bachelor's or master's), as authored by a student at Eindhoven University of Technology. Student theses are made available in the TU/e repository upon obtaining the required degree. The grade received is not published on the document as presented in the repository. The required complexity or quality of research of student theses may vary by program, and the required minimum study period may vary in duration.

General rights

Copyright and moral rights for the publications made accessible in the public portal are retained by the authors and/or other copyright owners and it is a condition of accessing publications that users recognise and abide by the legal requirements associated with these rights.

- Users may download and print one copy of any publication from the public portal for the purpose of private study or research.
- You may not further distribute the material or use it for any profit-making activity or commercial gain

Eindhoven University of Technology
Faculty of Biomedical Engineering
Biomechanics and Tissue Engineering

Determination of the Passive Transverse
Mechanical Properties of Skeletal Muscle
under In Vivo Compression

MSc Thesis

Niels Braakman
BMTE03.40

October 2003

Supervisors:
Dr. ir. C.W.J. Oomens
Ir. A. Stekelenburg
Prof. dr. ir F.P.T. Baaijens

Summary

As part of the start-up phase of the HUMOS II project, an attempt was made to determine the transverse mechanical properties of skeletal muscle tissue under in vivo loading conditions up to failure.

For this project a novel experimental set-up was designed and built to mechanically load the tibialis anterior muscle of anesthetized Brown Norway rats while the animals reside inside an MR scanner with a 6.3 Tesla magnet. The displacement of a fluid filled indenter was measured with high resolution MRI. The force was measured using strain gages mounted on a loading beam. A load of 0.5 N was applied for 2 hours. Immediately after load removal, a series of T_2 -weighted images were taken to detect damage. The T_2 -weighted MR images were taken based on the notion that water molecules have higher mobility in damaged tissue, and thus higher T_2 relaxation time, yielding high contrast to healthy tissue. The experiments were approved by the animal care committee of the University of Maastricht.

A three dimensional, geometrically non-linear finite element model was developed to describe the mechanical behaviour of the hind leg of the rat, comprising the muscles, skin, and bone. An Ogden model was used to describe the mechanical behaviour of skin and muscle. Contact elements were incorporated to permit sliding contact between indenter and the skin surface.

Results of the MRI experiments have shown that initial damage becomes visible on T_2 -weighted images approximately ½ hour after load removal and seems to start close to the bone.

Forces measured during experiments using the current set-up were much lower than expected based on the results of the simulation using reference material parameters. This indicates that the muscle has a lower stiffness than previously reported. A fit of the finite element model to the experimental test results yielded new, lower values for the Ogden material parameters. However, since the model is non-linear and the experimental results were obtained at only one level of loading, it is not currently known how well they will predict material behavior under different loading conditions. A further improvement is possible by the future combination of strain fields obtained by means of MR tagging experiments with the finite element model.

The methods employed here seem promising for determining the mechanical properties of the muscle tissue. Once operational, MR tagging measurements will provide strain fields and displacement data. Force measurement can be done accurately, both within and without the MR environment, and the apparatus is suited to providing a prolonged loading for damage assessment. Coupled with the finite element simulations, the data obtained will yield a further improvement of the material parameters reported previously.

Samenvatting

Als onderdeel van de begin fase van het HUMOS II project is getracht de transversale mechanische eigenschappen te bepalen van spierweefsel onder in vivo belasting, tot het ontstaan van schade.

Voor dit project is een speciale proefopstelling ontworpen en geconstrueerd om de tibialis anterior spier van ge-anaesthetiseerde Brown Norway ratten te belasten. Dit gebeurt terwijl de dieren zich in een MRI scanner met een 6.3 Tesla magneet bevinden. De verplaatsing van een, met vloeistof gevulde, indentor is bepaald met behulp van hoog-resolutie MRI. De belasting is gemeten met behulp van rekstrookjes gemonteerd op een buigbalk. Een kracht van 0.5N is gedurende twee uur aangebracht. Onmiddellijk na verwijderen van de kracht is een serie T_2 -gewogen MRI beelden gemaakt om de schade te bepalen. Hierbij is er van uit gegaan dat de mobiliteit, en daarmee de T_2 relaxatie tijd, van watermoleculen hoger is in beschadigd weefsel, waardoor dit een helderder beeld geeft op een MRI scan dan gezond weefsel. De experimenten zijn goedgekeurd door het animal care comitee van de Universiteit van Maastricht.

Een drie-dimensionaal, geometrisch niet-lineair eindige elementen model werd ontwikkeld om het mechanische gedrag van de achterpoot van de rat te beschrijven. Een viscoelastisch Ogden model is gebruikt om het gedrag van huid en spier te beschrijven. Contact elementen zijn in het model opgenomen om glijden tussen indentor en huid oppervlak mogelijk te maken.

Resultaten van de MRI experimenten hebben aangetoond dat beginnende weefsel schade al zichtbaar is ongeveer $\frac{1}{2}$ uur na het verwijderen van de belasting. De schade lijkt te beginnen in de buurt van het bot.

De krachten die gemeten zijn tijdens deze experimenten, zijn veel lager dan verwacht was op basis van simulaties met de referentie parameters. Dit duidt erop dat de spier een lagere stijfheid heeft dan eerder vermeld. Aanpassing van het model naar de nieuwe experimenten leverde een set nieuwe Ogden parameters. Het is echter niet bekend of deze parameters ook het mechanische gedrag bij andere belasting situaties goed zal beschrijven. De reden hiervoor is dat het model niet-lineair is, en de experimenten slechts zijn uitgevoerd bij een belastingssituatie. Een verdere verbetering is ook mogelijk door de toekomstige combinatie van rekvelen bepaald met behulp van MRI tagging met het eindige elementen model.

De methoden die hier gebruikt zijn lijken veelbelovend voor het bepalen van de materiaal parameters van spierweefsel. Als de MRI tagging experimenten eenmaal operationeel zijn, zullen deze rekvelen en verplaatsings gegevens leveren. Krachtmetingen kunnen al gedaan worden, zowel binnen als buiten de MRI omgeving. Het ontwikkelde instrument is geschikt voor het langdurig aanbrengen van belasting voor het bestuderen van het ontstaan van weefselschade. Gecombineerd met de eindige elementen simulaties, zal de verkregen data een verdere verbetering van de materiaal paramters tot gevolg hebben.

Contents

Summary	2
Samenvatting	3
1. Introduction	5
2. Muscle damage	6
3. Methods and Materials.....	8
3.1 Experimental - Numerical Method.....	8
3.2 Experimental Aspects.....	9
3.2.1 MRI.....	9
3.2.2 Force / Displacement Measurements: Indenter Unit.....	10
3.2.3 Protocol	12
3.3 Numerical Aspects	14
3.3.1 Reference Model.....	14
3.3.2 Modification of Current Model to Fit New Experiments	16
4. Results	18
4.1 MRI	18
4.2 Force / Displacement Measurements.....	20
4.3 Comparison Experimental – Numerical Work.....	21
5. Discussion and Conclusions.....	24
6. Recommendations.....	28
Acknowledgements	29
References.....	30

Appendices

Appendix A MRI basics	33
Appendix B MRI Slice Orientations	37
Appendix C Overview of the Experimental Set-up.....	38
Appendix D Indenter Unit Design.....	39
Appendix E Product Data Sheet - Ertalon 66 GF30	40
Appendix F Cam Design.....	42
Appendix G Indenter Unit: Maximum Strains	43
Appendix H Strain Gages.....	45
Appendix I Signal Measurement.....	47
Appendix J Strain Gage Calibration	49
Appendix K Viscoelastic Ogden	51

1. Introduction

Before bringing a new product to market, the automotive industry needs to make sure that it conforms to modern safety standards. Car safety can be tested in a variety of ways, of which the most commonly known makes use of the crash test dummy. Another, less costly method to determine safety is by running computer simulations. As input for these simulations, an accurate description of the mechanical characteristics of the tissues of the (human) body is needed.

As part of the HUMOS (Human Modeling System) project a first attempt was made to incorporate some of these characteristics into a computer model. However, HUMOS lacked adequate description of the mechanical behavior/characteristics of (muscle) tissue.

In work package 3 of the EC funded project HUMOS II (GRD2-2001-50053) the knowledge on biomechanical behavior of soft tissues will be improved. The Eindhoven University of Technology is responsible for the determination of the transverse and longitudinal mechanical properties of skeletal muscle during loading up to failure. The transverse mechanical properties will be the main focus of the current project.

The goal of this project is firstly to develop an instrument capable of delivering detailed and accurate force and displacement data. It was decided that it must also be MRI compatible so that possible damage resulting from loading could be detected. All experiments will be done in vivo, using the tibialis anterior muscle of Brown Norway rats.

Secondly, an improved numerical model was needed to approximate in vivo measurements. For the purpose of parameter estimation the finite element model previously used in the work by Bosboom [05], will be altered to enable faster assessment of parameter variations.

Since force and displacement measurements will be coupled in this work, resulting parameters are thought to be an improvement of those previously reported.

2. Muscle damage

By the nature of their position in the body, skeletal muscles are frequently subjected to physical trauma [24]. Muscle tissue will be damaged if the magnitude of the applied load is high enough or the duration is long enough, e.g. after (severe) crush injuries, or after lying on a hard surface for extended periods of time [24]. Figure 2.1 shows the relation between pressure magnitude and duration of load

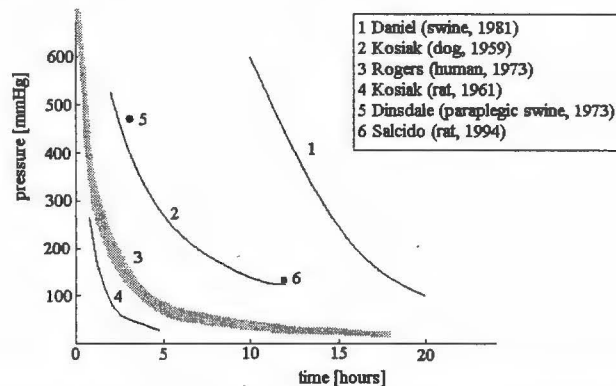


Figure 2.1: Risk curves with regard to tissue damage. Time/pressure combinations above the curve result in tissue breakdown. Adapted from [42].

The mechanical properties of skeletal muscle will change as a result of damage: Damage is initiated locally, so data on local deformation is essential for understanding the cause of muscle damage. Muscle damage and adaptation are initially local phenomena at the level of individual cells (see figure 2.2). To find a damage threshold for skeletal muscle it is necessary to know how external loads are transferred to local loads within the tissue. In order to study local muscle loading, numerical muscle models have been developed. To simulate realistic 3D muscle deformation, these models should have a realistic 3D geometry, since deformation in transverse direction is not negligible. Such a model, combined with experimental results, offers a solid tool to improve insights in the mechanics of muscle damage [17], [25], [42].

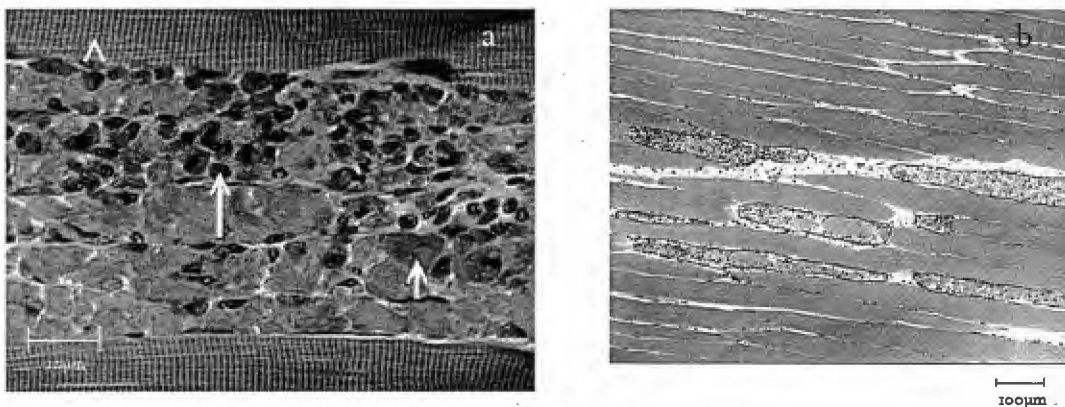


Figure 2.2: (a) Longitudinal histological section of muscle showing the typical cross-striated appearance of skeletal muscle (arrowhead), a loss of cross-striation of muscle fibers in the damaged area (small arrow) and the infiltration of mononuclear cells (large arrow). (b) Detection of the damaged area within part of a slice. Adapted from [05]

Previous work has mainly focused on the determination of muscle damage in the form of pressure sores. There, MRI was used to determine muscle damage after prolonged transverse loading. Histological data obtained after testing was compared to data obtained

through MRI. It was found that the location of higher signal intensity in MR is in agreement with the location of muscle damage assessed in the histological examination; see figure 2.3 [05], [06], [43]

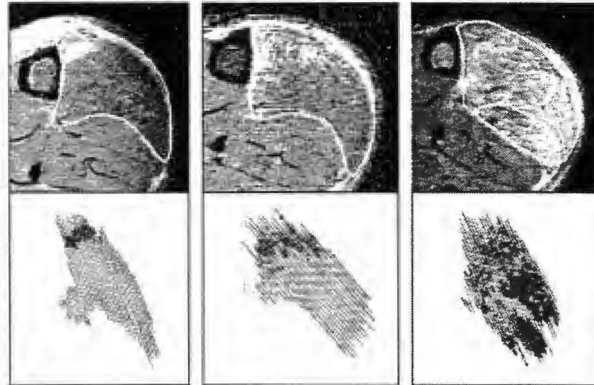


Figure 2.3: Damage in transverse histological slices (bottom) and T_2 -weighted MR images in the center plane of the indenter. Adapted from [05], [42]
For more information see section 3.2.1 and Appendix A.

Muscle damage was defined as loss of cross-striation and infiltration of mononuclear cells. Evidence of this trauma is visible 24h after loading occurred (figure 2.2). Kosiak (1961) found that intense pressures of short duration are as injurious to tissues as low pressures applied for longer periods (see figure 2.1) [42]. Muscle damage after impact, short duration – high magnitude loading, is likely of a different type than that occurring after prolonged periods of loading at lower load magnitude.

3. Methods and Materials

As mentioned in the introduction, all experiments were performed on rats. The muscle of interest here is the left Tibialis Anterior (TA) muscle, a muscle which has been the subject of several previous studies [05][17], [25], [42] [44]. In this chapter the experimental and numerical aspects of the research will be discussed.

3.1 Experimental - Numerical Method

A common method to determine material mechanical characteristics is to subject specially machined samples to tensile loading. This uniaxial strain test makes use of a well-defined basic shape; the sample is designed in such a way that loading should lead to a homogeneous strain distribution in the central region. However, standard ways for quantitative determination of material parameters result in insoluble problems when applied to complex solids [21]. When performing a uniaxial strain test it is assumed that the central part of the sample undergoes uniaxial loading (figure 3.1a) and its properties are representative for the material as a whole [21]. While these are valid assumptions for a homogeneous material, biological material is not homogeneous. For complex biological materials, standard testing often fails to give satisfactory results. Extreme anisotropy produces inhomogeneous stress and strain fields (figure 3.1b), while standard testing requires these to be homogeneous [40]

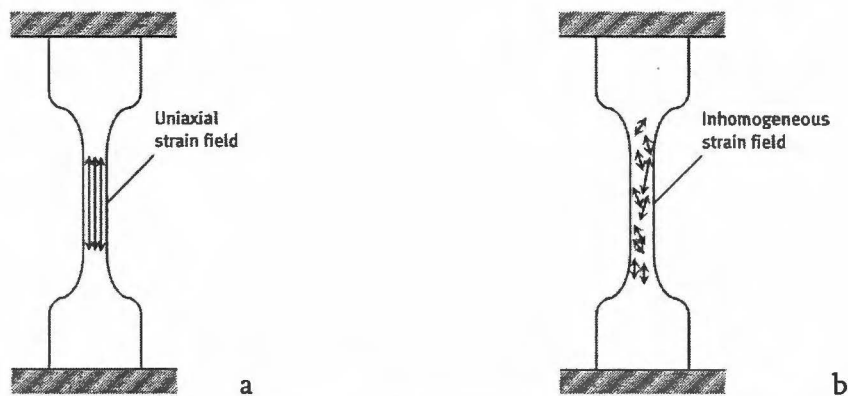


Figure 3.1: Strain distribution in a homogeneous (a) and complex / biological (b) sample. Reproduced from Braakman [08]

When characterizing complex materials better results are obtained when the strain distribution in the entire sample is recorded (Peters, 1987). Using a mixed numerical-experimental method, the deformation data of the entire sample is measured [21], [40]. The key point for material characterization is the combination of displacement field measurement, finite element modeling (FEM) and parameter estimation. Using FEM and an adequate constitutive model the experimentally determined deformation can be mimicked and, in doing so, the model's parameters can be determined [21], [28], [40]

3.2 Experimental Aspects

In the following sections the method used to determine the force-displacement characteristics and the methods that can be used to determine strain fields and damage to muscle tissue *in vivo* will be discussed. Finally, the protocol used in the experiments will be given.

3.2.1 MRI

Nuclear Magnetic Resonance (MR) is a technique that is based on the magnetic properties of the nuclei of hydrogen atoms (protons) naturally present within the body. The protons have a spin, which produces a small magnetic field, so that they behave like small magnets. When a subject is positioned within the bore of a cylindrical, superconducting magnet, the protons are aligned by the external magnetic field of the MR system in such a way as to create a measurable magnetization of the body, the strength of which depends on the density of the protons in the tissue. In order to produce an image, the magnetization of the body is disturbed by applying a radio-frequency (RF) pulse. As the magnetic field returns to its original orientation, it produces a signal that can be detected by a receiver coil and used to create an image [33], [43].

An MR system basically consists of the following components: A large magnet that provides the static magnetic field; Radio-frequency coils transmit and receive the radio signals; Magnetic field gradient coils provide the spatial localization of the signal and with the aid of a computer the radio signal is reconstructed into the final image [43].

For this research a custom set-up was built to house the experimental animal, in this case a rat, during testing inside the 6.3 Tesla MR Scanner of the faculty of Biomedical Engineering (see figure 3.1). The set-up is described in more detail in section 3.2.3 and appendix C.

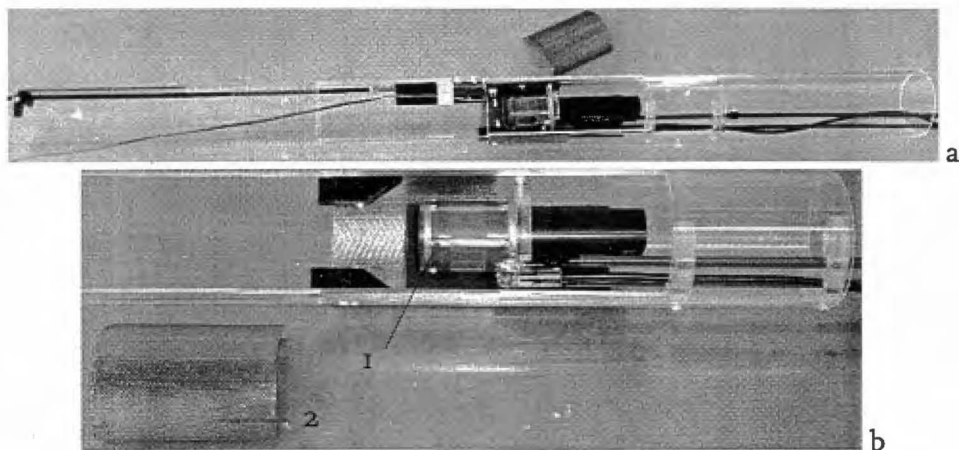


Figure 3.1: Experimental set-up; (a) completely assembled, and (b) a close-up of the RF Coil (1) and RF Shield (2).

MR tissue tagging with dynamic MR imaging is a rapidly developing technique for the quantitative, non-invasive evaluation of displacement within muscle with a high spatial and temporal resolution [29]. The technique works as follows: Over a period of milliseconds the magnetization of tissue is periodically modulated with a grid pattern, thus forming tags. If the tissue moves, the magnetization tag will move along with it, directly revealing the displacement of the tagged region in the subsequent image, see

figure 3.2 [01], [02], [38], [45]. Mathematical techniques can then be used to reconstruct a 3-dimensional deformation field from tag positions on MR images [29]. Also, detailed motion of the tissue can be deduced by analyzing the deformation of taglines found within these images [43].



Figure 3.2: Coronal in vivo MR tagging images of a mouse hind limb leg (a) in rest and (b) during contraction by stimulation of the sciatic nerve. Reproduced from [43]. See Appendix A for an explanation of the orientations.

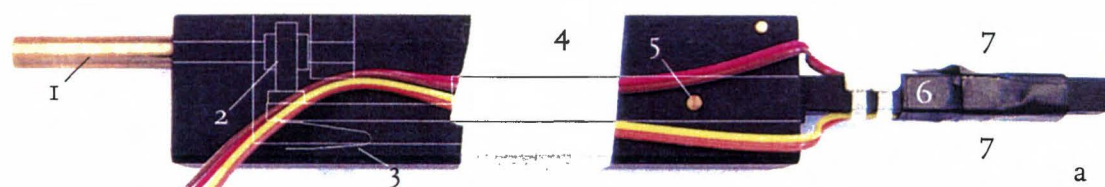
In addition to being able to determine strain fields and deformation in the muscle, MRI can be used, as shown in the work by Bosboom [05], [06], to detect, in vivo, damage to muscle tissue. The technique used for this is T_2 -weighted MR imaging;

After excitation, the MR signal present in the xy-plane will decay exponentially to zero over time. The time required for 63% of the signal to disappear irreversibly is called the T_2 relaxation time or the transverse or spin-spin relaxation time. Small molecules (e.g. liquids) exhibit a long T_2 , while larger molecules (e.g. lipids) tend to have a shorter T_2 . The exponential signal decay due to T_2 relaxation attenuates the signal from fluid and edema more slowly than the signal from fat, muscle, or normal connective tissues. Therefore, fluid and edema appear bright on T_2 -weighted MR. Fat displays moderate intensity whereas muscles are hypointense. Tendons, ligaments and cartilage appear dark. T_2 weighted images provide excellent contrast between normal and abnormal tissues. T_2 is related to the coherence of a group of protons, and is a measure of the local molecular mobility. Increased water mobility (for example due to muscle damage) leads to increased T_2 relaxation time [52]. See Appendix A for more detailed information.

3.2.2 Force / Displacement Measurements: Indenter Unit

For the purpose of mechanical loading of the muscle and measurement of reaction forces, an indenter unit was designed. The unit was required to be able to impose a fixed displacement, while measuring the reaction forces of the muscle. In addition, the application of the load must take place at high speed, to enable MR tagging for the determination of displacements and strain within the muscle.

The final unit design is shown in figure 3.3. More detailed information can be found in Appendix D. The housing (4) and bending beam (6) of the instrument are constructed from Ertalon 66 GF30, a glass fiber reinforced polymer (see Appendix E). The use of this material ensures high stiffness, while being fully MR compatible.



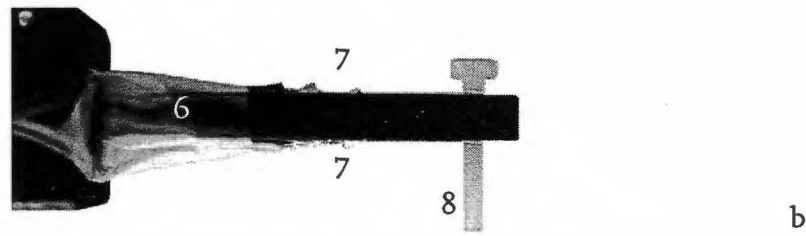


Figure 3.3: The indenter unit (a, b) – drive shaft (1), cam (2), spring (3), housing (4), hinge point (5), loading beam (6) with strain gages (7) and a Ø3mm fluid-filled indenter pin (8).

The indenter pin (8) is a Ø3mm PMMA screw with a hollow tip filled with water. The cam (2), drive shaft (1) and points of high stress, such as the hinge point (5), are constructed from brass. The spring (2) is made of copper. Reaction forces are measured using strain gages attached to the bending beam (7). The strain gages (CEA-06-250UW-350), are manufactured by Vishay Measurements Group [48]. They were attached to the bending beam by means of Loctite Cyano-Acrylate glue. By using two strain gages, attached to a ½ Bridge of Wheatstone, temperature effects can be compensated for [49] (Appendices H, I)

Measurements are done using a Peekel Instruments Carrier Amplifier System consisting of MCA130, CA100 and CCA100 components. The output signal is logged on a pc running LabView (see appendix I).

In order to make the MR tagging experiments possible with the same set-up used for force measurements, the indenter needs to move from its initial position to its maximum depth in the shortest time possible. To ensure the quality of the images, this would ideally be in the order of 10ms. The drive system shown in figure 3.4 was designed to allow this.

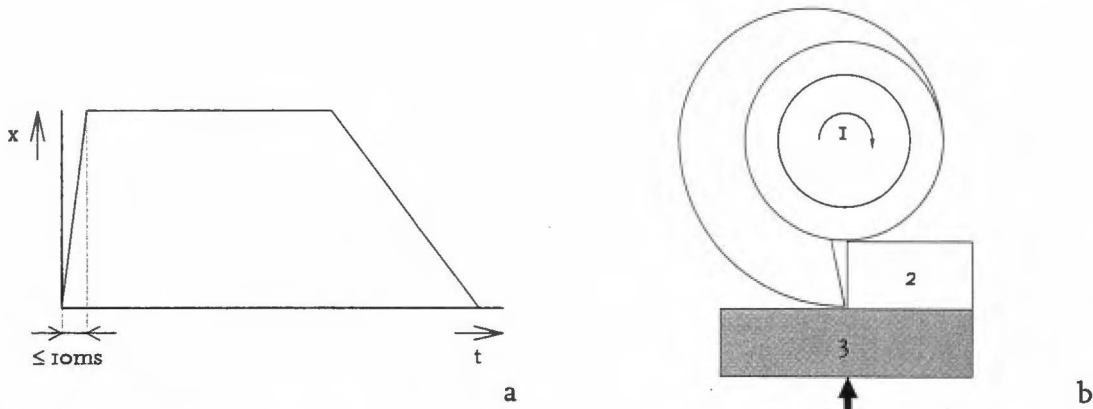


Figure 3.4: When using the MR tagging technique, it is imperative that the full displacement is reached well before the projected grid fades. For best results this should be 10ms or less (a). The combination of the cam (b) with the arm held against it by means of a very stiff spring makes this possible. The components listed in (b) are: 1) cam, 2) brass plate, 3) rear end of the bending beam

The cam (figure 3.4b) is fitted to a driveshaft, which can be powered by a computer-controlled motor. Upon rotation, the cam (1) presses against a brass plate (2) attached to the rear end of the bending beam (3). A very stiff spring underneath the arm supplies the force necessary to prevent separation, and also ensures that the prescribed displacement of the indenter pin is attained. Once the tooth of the cam passes over the edge of the

plate, the arm is immediately displaced upwards, over a distance x . The magnitude of the displacement depends on the cam used; several cams were designed, each with a different height (appendix F). These cams can be exchanged relatively easily. The unit is able to accurately measure applied loads. The R^2 value of the calibration curve is in the order of 0.99. Calibration curves and details of the calibration of the unit are shown in appendix J.

3.2.3 Protocol

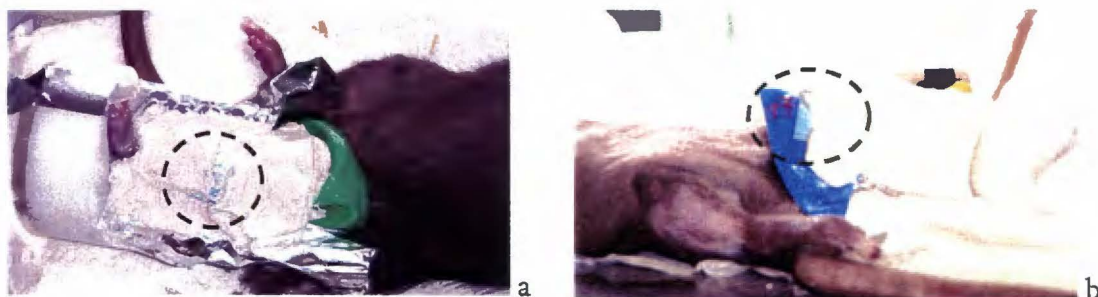
Experiments were performed on the left tibialis anterior (TA) muscle of three female Brown Norway rats, aged approximately 30 weeks and weighing 200-220 grams. The rats were anaesthetized initially by isoflurane inhalation, followed by subcutaneous injection of xylazine (2.5 $\mu\text{l}/\text{gr}$) and intramuscular injection of ketamine (1 $\mu\text{l}/\text{gr}$). Body temperature was maintained at 35-37 $^{\circ}\text{C}$ using a heating pad. The Animal Care Committee of the University of Maastricht approved the experiments.

The following steps were followed in preparation for testing:



Figure 3.5: The rat after anesthesia (a), shaving the left rear leg (b). Once shaved (c), the leg is dressed in balloons.

Once fully anaesthetized, the left rear leg is shaved to expose the area where the TA muscle is located (figure 3.5b & c). When doing this, care should be taken not to damage the skin. Following this, the desired location is marked on the muscle, and the leg is dressed in balloons cut to size (figure 3.5d). The balloons serve to protect the leg during fixation.



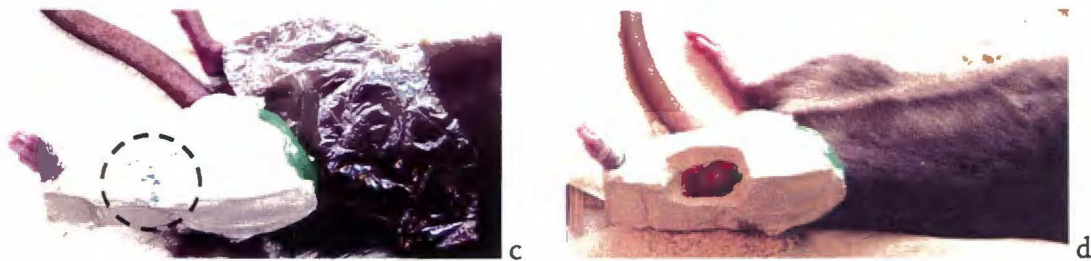


Figure 3.6: Fixation of the leg: application of plaster inside the mold (a), plastic brace inserted into the plaster to aid in positioning of the leg inside the experimental setup (b), the fixated leg before (c) and after (d) exposing the desired area.

The dressed leg is placed into a specially designed mold and plaster cast is applied (figure 3.6a). The highlighted area shows where a marker was attached to the leg to facilitate the localization of the test area. Before the plaster has set, two plastic braces are inserted on either side of the leg (figure 3.6b). As soon as the plaster is firm, but not yet completely solid, the leg and cast are removed from the mold (figure 3.6c). If necessary additional plaster is applied. Once the plaster is firm enough to handle, a hole is cut into it, starting at the marker. Finally, the test area is exposed by cutting away the protective covering provided by the balloons (figure 3.6d).

When this stage in the preparation is reached, the animal is transferred to the experimental set-up.

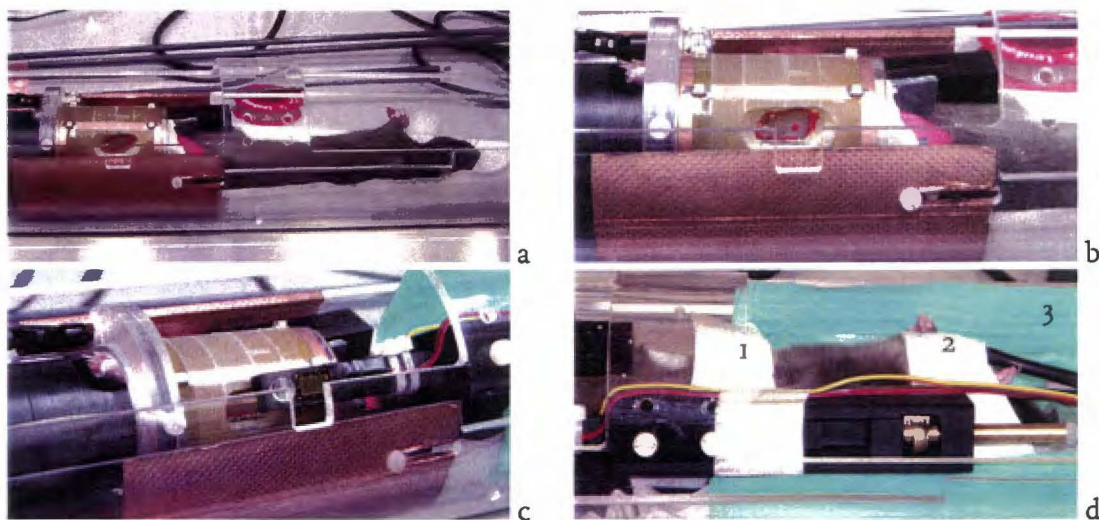


Figure 3.7: The rat inside the experimental set-up (a), the leg positioned inside the RF coil by means of the braces, the indenter unit positioned over the muscle (c), rat hooked up to monitoring apparatus (d); respiration monitor attached to the abdomen (1), a pulse-oxy meter attached to the front leg (2). Body temperature is controlled by means of a heating pad (3).

Inside the setup (see also Appendix C) the fixated leg is positioned and clamped in place within the RF coil (figure 3.7a & b). Following this a heating pad is placed around the animal, to control its body temperature once inside the MRI. Heart- and respiration rate are monitored using respectively a pulse-oxymeter attached to a front leg and a respiration monitor attached to the abdominal area (figure 2.7d). For the duration of the tests the animal is kept on respiration and kept anaesthetized using a 1:1 mixture of O_2 and NO_2 initially, which is supplemented with isoflurane as time progresses.

Once the animal is connected to the monitors and respiration, the indenter unit is placed in position (figure 3.7c & d). Before the start of the experiment the arm needs to be in the

highest position, and the indenter pin just touching the skin (thereby just registering a force on the signal amplifier).

At this point there are three possibilities on how to proceed; the next steps in the protocol depend on the type of experiment that is to be run:

- For simple force measurements, the setup can be kept outside the MRI, and multiple tests can be done at intervals of several minutes, allowing the muscle time to recover. To ensure correct measurement, the strain gages are calibrated just before the start of the experiment and checked upon completion by applying a known force.
- For MR Tagging experiments, the setup will need to be placed inside the MR environment, and the displacement of the indenter and its triggering controlled by computer.
- For damage evolution measurements, again the setup will need to be placed inside the MR environment. Consequently a $t = 0$ scan will be made (as reference), followed by gradual loading of the muscle. Once the full load is applied it is left for approximately 2 hours. After unloading another scan is made to identify possible damage to the muscle tissue. Upon completion of this scan, the rat can be removed from the setup and revived. After 24h the entire procedure will be done again, with the exception of force application, to study the evolution of damage. Animals are sacrificed immediately after the second set of measurements.

3.3 Numerical Aspects

In order to obtain material parameters for the TA muscle, a constitutive material model will need to be chosen. Once implemented in a finite element simulation, material parameters can be determined by fitting the results of the simulation to results obtained experimentally. This section will discuss the material model used, as well as the finite element simulation, and its adaptation for use in current work.

3.3.1 Reference Model

To assess the local mechanical conditions in the muscle during the animal experiments, finite element simulations were performed using the software package MARC (MSC.Marc, 2000). The model used to this end is the same one used in the work of Bosboom [05]. It will be used as a basis for new simulations, and previously reported material parameters provide initial estimates for parameter estimation in the new situation.

This model consists of a section of muscle and skin surrounding the area the indenter makes contact. The geometry of the model was based on MR images. As the tibialis anterior muscle forms a functional unit with the extensor digitorum longus muscle, surrounded by a thin fascia, these two muscles were modeled as one structure, hereafter referred to as muscle. The skin thickness was measured *ex vivo* and modeled as a 0.7 mm thick layer covering the muscle. The rats had little subcutaneous fat; therefore this layer was not modeled separately. The muscle and skin were modeled with respectively 2592 and 1408 first order hexahedral elements (figure 3.8). These elements were based on the Herrmann variational principle to prevent locking due to incompressibility. To describe the material behavior of skin and muscle an incompressible Ogden model was employed.

The strain energy W of this model is given by [05], [31], [32], [35]:

$$W = \sum_{n=1}^N \frac{\mu_n}{\alpha_n} (\lambda_1^{\alpha_n} + \lambda_2^{\alpha_n} + \lambda_3^{\alpha_n} - 3) \quad (3.1)$$

Where W is a function of the principal stretch ratios, λ_i , and the material parameters μ_n [MPa] and α_n [-]. Viscoelasticity is implemented in this model in the following manner [05]:

$$\mathbf{S} = \left(\mathbf{I} - \sum_{m=1}^M \delta_m \right) \frac{\partial W}{\partial \mathbf{E}} + \sum_{m=1}^M \int_0^t \delta_m \frac{\partial W}{\partial \mathbf{E}} e^{-(t-\xi)/\tau_m} d\xi \quad (3.2)$$

where \mathbf{S} is the second Piola-Kirchhoff stress, \mathbf{E} is the Green-Lagrange strain and δ_m [-] and τ_m [s] are viscoelastic material parameters. First order models were used for the viscoelastic behavior of skin and muscle; i.e. $N = 1$ and $M = 1$.

The material parameters used for muscle and skin are listed in table 3.1

Table 3.1: Applied Ogden parameters of the incompressible viscoelastic Ogden model ($N = 1$ and $M = 1$) for skin and muscle.[05]

Tissue	μ [MPa]	α [-]	δ [-]	τ [s]
Muscle	0.0156	21.4	0.55	6.0
Skin	0.016	10.0	0.50	20.0

The tibialis anterior muscle is bound to the tibia with fascia. Therefore all nodal displacements of the muscle were suppressed on the surface in contact with the tibia. In addition, the muscle is supported by the membrana interossea, a stiff, collagenous membrane between the tibia and fibula. Displacements of the muscle along this interface were also suppressed. Contact between the indenter and the skin, and between the skin and muscle was modeled by applying a direct constraint method. The finite element model consists of three contact bodies: a rigid indenter, a deformable skin layer and deformable muscle tissue. Relative sliding of the skin along the muscle and indenter was enabled, while friction was neglected. The tissues were incrementally loaded (in 20 steps) by prescribing the motion of the rigid indenter. The total displacement was chosen such that the force on the indenter corresponded to the 2N applied during animal experiments.

Initial simulations were run on a model where all displacement of the muscle area in contact with both the tibia and membrana interossea was suppressed (figure 3.8a). An alternative model was also employed, where the membrana interossea was included (figure 3.8b). Since the membrane consists mainly of collagen, material properties of ligament were taken as a starting point for its properties. To avoid a high aspect ratio of the three-dimensional elements, the membrane was modeled as a 1mm thick layer. As this is 25 times thicker than its actual thickness, the E-modulus was adjusted to 1/25 of literature values, so that correct behavior under bending would be approached; i.e. $E = 10$ MPa and $\nu = 0.5$.

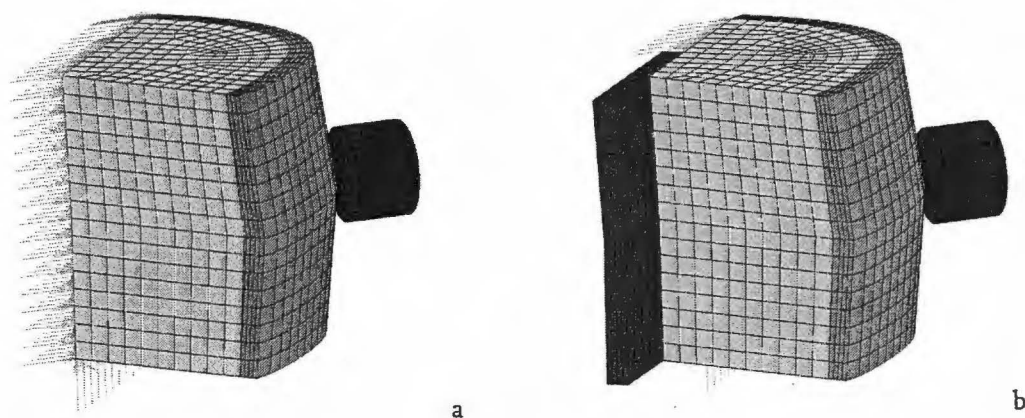


Figure 3.8: 2 Different models designed by Bosboom [05] - With one entire side of the TA muscle fixed (a), and one where the membrana interossea is modeled (b)

This model has some drawbacks in its current form, however; computational time is in the order of 100 hours, and when the material parameters are varied, convergence is often not reached.

3.3.2 Modification of Current Model to Fit New Experiments

As mentioned in the previous section, simulations can take more than 100 hours to complete. For purposes of parameter estimation, a shorter calculation time is desirable.

There are a couple of options that might speed up the process: The first is to simplify the problem, in this case by combining the muscle and skin into a single contact body. Since sliding between muscle and skin is prevented in this case, there are some differences in stress-strain distribution along the interface; the magnitudes in the two cases do not show significant differences. Overall, however, the differences are considered to be of less importance than the increased simulation speed; the changes implemented here reduced the calculation time by about 75%, simulations now run in about 30 hours. While this is an improvement, it is still too long.

The next step was to use a different solver in the simulation. In the reference simulations a direct solver was used; this was changed to an iterative solver with an incomplete Cholesky preconditioner. The resulting simulations ran to completion in 1-2 hours, a marked improvement. To verify whether results obtained by means of the iterative solution method were the same as those obtained through direct solution of the problem, two simulations were run, the only difference between them being the choice of solver.

Results were compared, and the relative error in force and displacement over time was determined:

$$\text{relative error} = \frac{\text{direct method} - \text{iterative method}}{\text{direct method}} \quad (3.3)$$

Results are plotted in figure 3.9.

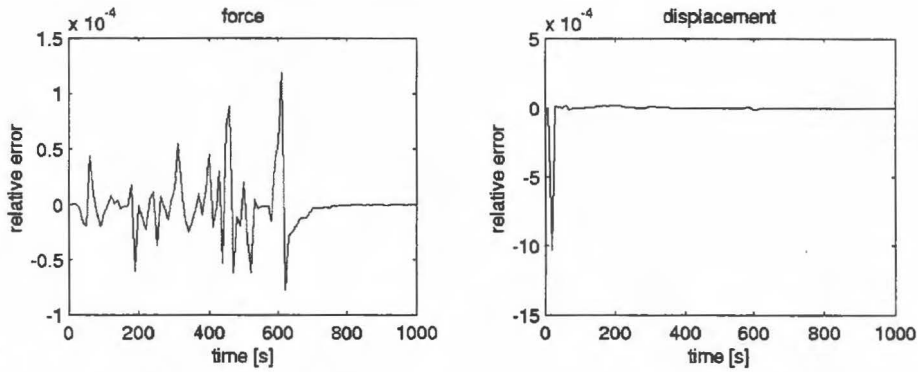


Figure 3.9: Relative errors in force and displacement over time; comparison of direct and iterative solvers

The differences are minimal, so it can be argued that the iterative method can be used instead of the direct method. The advantage of this is the major gain in calculation speed; 1-2 hours per simulation using the iterative method and the modified contact body, compared to 12-20 hours with reference mesh but iterative solver, 30+ hours for the direct method with modified contact bodies and 120+ hours for the direct method with reference mesh.

Other modifications to the simulation include the increased number of increments, or time steps, used. The original simulation used 20 increments, which led to convergence problems upon varying parameters, or speed of load application. To simulate the impact loading as imposed by the new indenter unit, the load application time was reduced to 0.1 second, compared to 400 seconds previously. The highest number of increments (40 in total) was used in the initial displacement step, and just beyond, to ensure accuracy and convergence. Once equilibrium is reached, time steps can be greater, as the changes from one point to the next will be smaller.

4. Results

4.1 MRI

A series of MRI scans were made to assess muscle damage. To this end T_2 -weighted imaging was used, as it has been shown [05] that using this technique tissue damage can be determined. The sequence parameters were as follows: field of view, $30 \times 30 \text{ mm}^2$; matrix size, 128×128 ; slice thickness, 1mm; TR, 4s; TE, 25ms. The first series of images (figure 4.1) were taken during loading (a-d) and 30 minutes after unloading (e-h). The load applied was between 0.5 and 0.6 N over a period of 2 hours. Indentation was approximately 4.2mm. Post-loading images were taken 30 minutes after load removal.

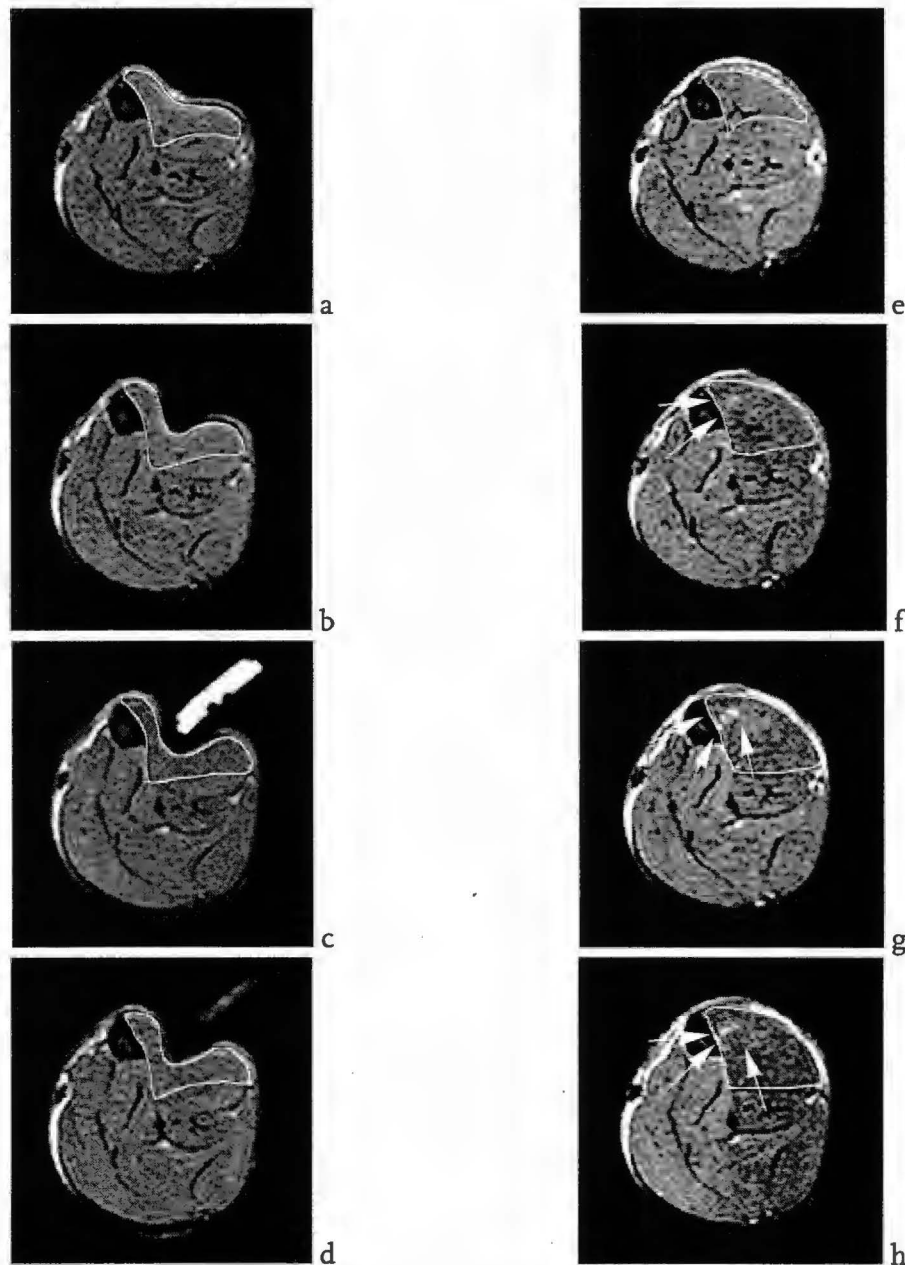


Figure 4.1: Subsequent transverse slices of the leg during loading (a-d), and 30 minutes after the removal of the load (e-h). The contour of the muscle is shown in white. Arrows indicate areas which seem to be damaged; cloudy white area inside the muscle. The white body shown in image c is the water-filled tip of the indenter.

As seen in figure 4.1 e-h, the area around the indenter shows what appears to be damage, starting at the bone and moving outwards (see arrows). It is only present in those areas which experienced the greatest loading (slices f-h), areas further away from the loaded area are clear of damage (slice e).

The second series of scans was also taken to assess tissue damage due to prolonged loading. The load history of the muscle in figure 4.2 is somewhat different to the one in figure 4.1; prior to the first scan a series of force/displacement measurements were done using the indenter unit with its cam driven displacement.

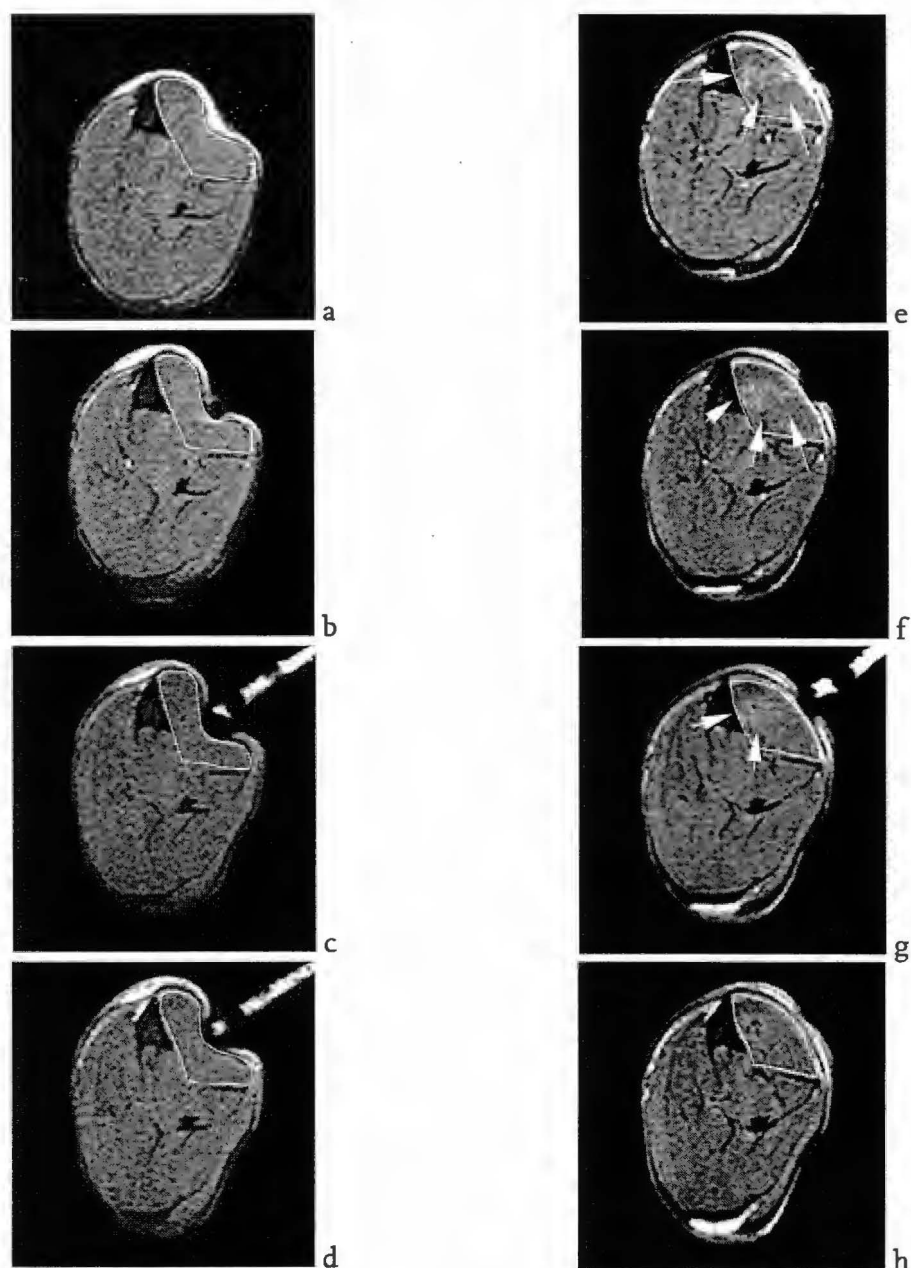


Figure 4.2: 2nd series of loading experiments. Images taken after a series of 5 force measurements. Indentation was lower than in the experiments shown in figure 4.1. Images a-d were taken shortly after the final load application. Images e-h were taken shortly after the force experiments. Total loading time here had been no more than 30 minutes, but again there appears to be some damage in the area around where the indenter impacted the muscle.

Again, there seems to be some damage visible in the images, although it is much less defined than in the previous series. Of interest is that the total load time here was perhaps

30 minutes. The damage is likely to have been caused during the force measurements; for each force measurement, the indenter impacts with the muscle. In this series 5 force measurements were done.

The magnitude of the load wasn't large enough to cause lasting damage; scans made 18 hours after load removal no longer show evidence of tissue damage.

4.2 Force / Displacement Measurements

Force measurements were done on two rats; both series of tests used a 3mm cam, which equals an actual indentation of 2.75mm as measured by MRI. The sample rate used in the 1st series was 1/s, while the 2nd series used a rate of 10/s. The initial load and its ensuing drop are best captured using the higher sample rate, as can be seen in the figure below.

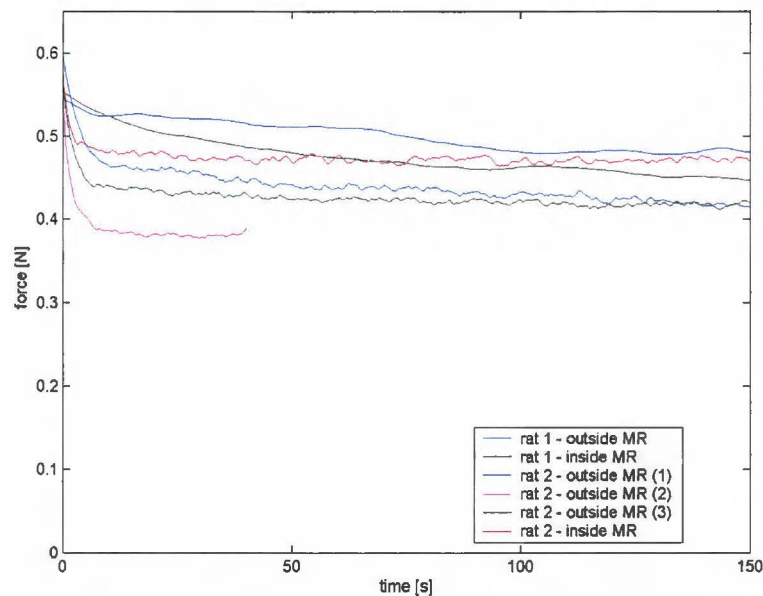


Figure 4.3: Experimentally determined forces. The first series (rat 1) used a sample rate of 1/s, the second used a sample rate of 10/s. Results shown here have been filtered to remove noise

Initial loads are in the 0.55 - 0.6N range, and in equilibrium the force lies between 0.45 and 0.5N. These results are lower than expected; the values predicted by the reference model and parameters were in the range of 1.8 - 2 N. These results suggest the muscle has a lower stiffness than previously reported.

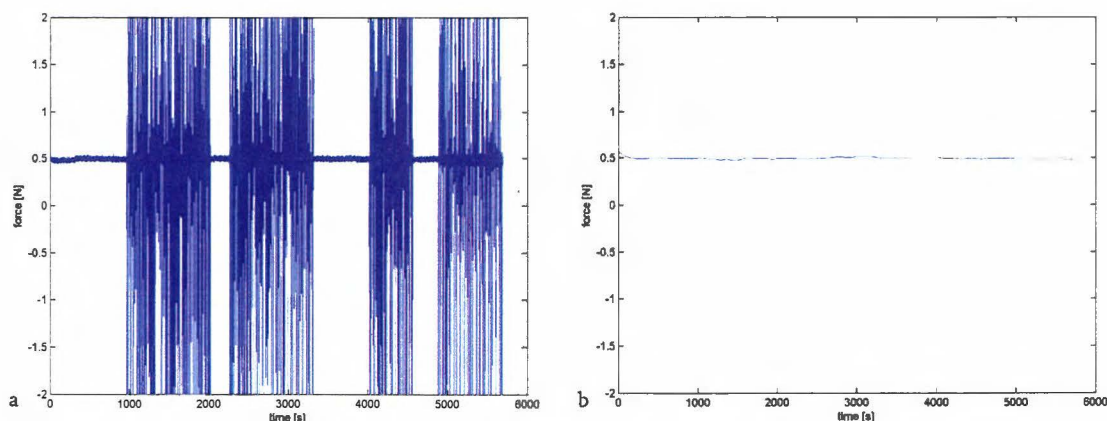


Figure 4.4: An example of the effects of MRI measurements on the force readout (a). Filtering the measurement removes all influences (b)

As shown in figure 4.4, the rapidly modulating RF pulses during MRI scanning distort the signal of the force measurements. While the distortions are considerable, the forces measured during the intervals that no scanning took place are equal. This is also verified by filtering the signal (figure 4.4b).

4.3 Comparison Experimental – Numerical Work

The first step in fitting the simulated forces to those measured experimentally is understanding the Ogden equations (section 3.2.1) which describe material behavior of the model. The stress relation is given below:

$$\mathbf{S} = (\mathbf{I} - \delta) \frac{\partial \mathbf{W}}{\partial \mathbf{E}} + \int_0^t \delta \frac{\partial \mathbf{W}}{\partial \mathbf{E}} e^{-(t-\xi)/\tau} d\xi \quad (4.1)$$

At the moment of initial force application ($t = 0$), the above equation simplifies to

$$\mathbf{S} = \frac{\partial \mathbf{W}}{\partial \mathbf{E}} \quad (4.2)$$

At this moment, the only Ogden parameters that play a role are those that are part of the strain energy equation, which is given by ($N = 1$):

$$\mathbf{W} = \frac{\mu}{\alpha} (\lambda_1^\alpha + \lambda_2^\alpha + \lambda_3^\alpha - 3) \quad (4.3)$$

Stress at $t = 0$ can only be modified by modifying μ and/or α .

Once equilibrium is reached ($t \rightarrow \infty$), the stress equation equals:

$$\mathbf{S} = (\mathbf{I} - \delta) \frac{\partial \mathbf{W}}{\partial \mathbf{E}} \quad (4.4)$$

The drop in stress levels depends on the value of δ . The parameter τ determines the viscoelastic relaxation rate.

It was assumed that these same relations could be used to simulate the forces measured experimentally.

The parameters μ and α were used to position the peak force resulting from the simulation over the peak force measured in experiments. However, since the material exhibits non-linear behavior, different load histories are required to determine both μ and α . Since measurements were only taken in experiments using the 3mm cam, it is not yet possible to determine the non-linearity. For this reason, the lowest value of α found in literature was taken, and only μ was estimated.

To determine δ , the maximum and equilibrium forces were taken of all experiments. From the ratio δ was determined:

$$F_{eq} = (\mathbf{I} - \delta) \cdot F_{max} \quad (4.5)$$

or for δ :

$$\delta = 1 - \frac{F_{eq}}{F_{max}} \tag{4.6}$$

The peak force (at $t \approx 0$) of each measurement was disregarded, as it was likely caused by inertia of the muscle. The table below lists the remaining maximum and equilibrium forces and the resulting values for δ .

Table 4.1: Peak and equilibrium forces as determined experimentally, and the resulting estimate for δ

Experiment #	1	2	3	4	5	6	average
F_{max} [N]	0.63	0.58	0.58	0.59	0.57	0.56	0.59
F_{eq} [N]	0.42	0.39	0.43	0.48	0.48	0.47	0.45
δ [-]	0.33	0.33	0.26	0.19	0.16	0.16	0.24

Using the value of 0.24 for δ , literature values for α , and varying μ , the simulation peak and equilibrium forces were fit to experimental data. Once a value for μ was found, τ was varied until the initial slope of the force graph resembled those of the experimental results. The final model yielded the following graph:

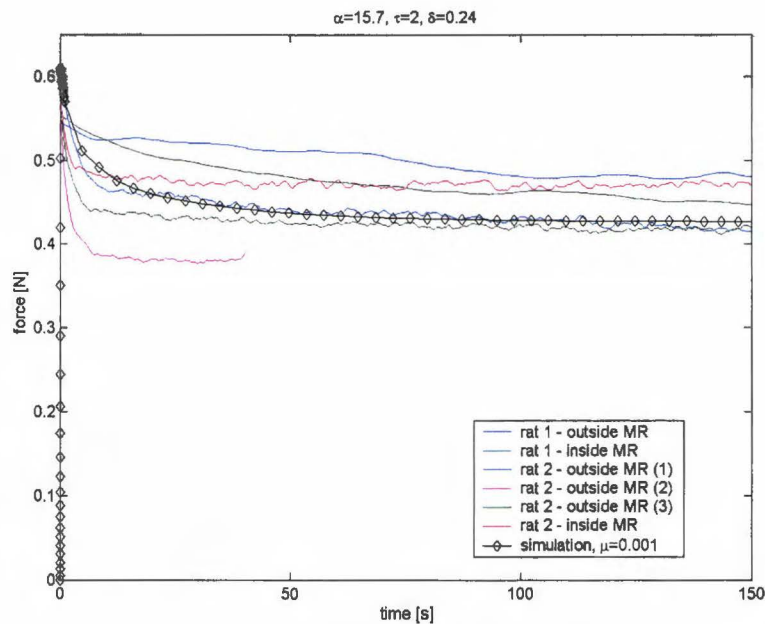


Figure 4.5: Fit of the finite element simulation forces to the experimental data.

The final estimates of the Ogden parameters, which were used in above simulation, are given in table 4.2.

Table 4.2: Comparison of the material parameters used in previous and current work.

Ogden parameters	μ [MPa]	α [-]	δ [-]	τ [s]
Previous work [05]	0.0156 ± 0.0054	21.4 ± 5.7	0.549 ± 0.056	6.01 ± 0.42
Current work	0.001	15.7	0.24	2

Note: closer inspection of equation 4.1 will show that the dimensions do not agree, meaning this is not the correct form of the equation. Marc simulations, however, behave exactly as described here. This might indicate that the viscoelastic part of the Ogden model is implemented incorrectly in the MSC.Marc software. See appendix K for the correct form of the viscoelastic Ogden model.

The final numerical model was compared to results obtained from the MRI study. The comparison in figure 4.6 shows that the deformed geometries of the model and the actual muscle have some differences. First off, the indenter is placed lower on the muscle in the experiments; secondly the angle of the indenter differs slightly. And finally, the finite element model of the muscle seems to have a larger cross-section than the actual muscle.

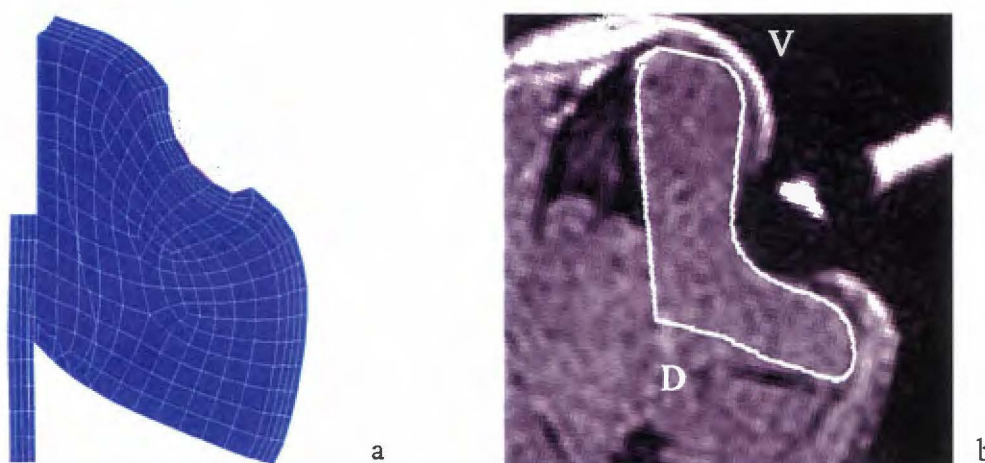


Figure 4.6: comparison of deformed geometries: simulation (a) vs. experimental (b)

The maximum shear strains, which are thought to be responsible for tissue damage [05], were calculated. Shear strain distribution in the cutting plane of the indenter is plotted in figure 4.7a. Figures 4.7b and c show the areas which received the highest loading. The dashed lines indicate the damaged areas. These areas do lie in areas of high shear strain.

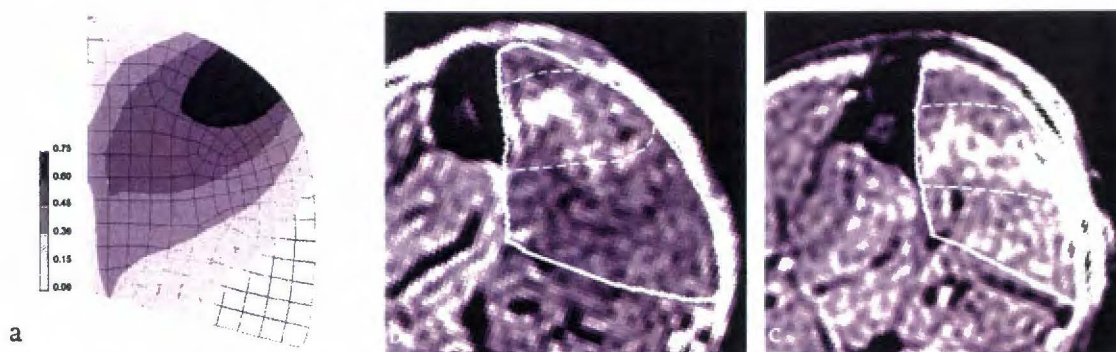


Figure 4.7: Areas of highest shear strains determined by simulation (a) compared to areas showing (possible) tissue damage in case of 2h loading (b) and after multiple impact loads (c)

5. Discussion and Conclusions

The methods presented here provide a valuable and accurate way for determining the force response of muscle tissue compressed by means of an indenter. The designed indenter unit can accurately measure these forces, both inside and outside the MR environment. It does have a small drawback, however.

Due to its design, the indenter pin does not move in an exact, straight line when indentation is prescribed (figure 5.1). However, since the indentation depth (x) is so much smaller than the length of the loading beam (L), the angle over which the pin rotates is relatively small; in order of 3 degrees for an indentation depth of 3mm. However, this angle results in a sideways displacement of about 1mm, assuming the indenter pin has a length of 20mm. Possible effects of this motion have not been taken into account in the modeling process.

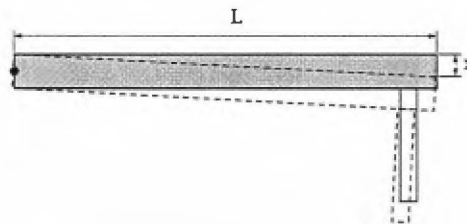


Figure 5.1: indenter displacement; both vertical and horizontal due to its design.

The carrier signal of the force measurements is influenced by the RF pulses of the MRI scanner. While the influence appears to be dramatic, the actual force reading remains stable, as can be seen from the filtered signal (figure 4.4).

Forces measured in current research were consistently lower than the forces predicted by simulations using Ogden parameters from previous work [05]. This implies that the stiffness of the muscle is lower than measured previously. The likeliest reason for this is the fact that Ogden parameters were previously estimated from experiments on a partially excised TA muscle (figure 5.2), which was compressed between two plates. Since the muscle wasn't in its natural state, and some dehydration is likely to have occurred, the stiffness could possibly be higher as a result.

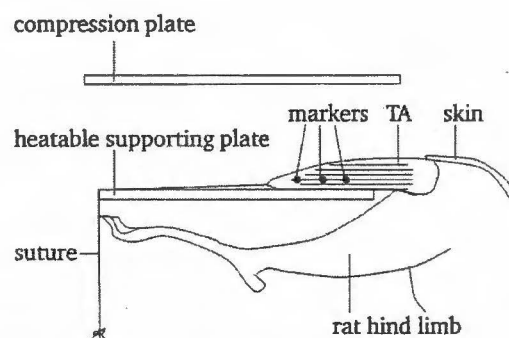


Figure 5.2: experimental method used previously to estimate the Ogden parameters [05]

Other possible factors that might influence the stiffness are the sex and age of the test subjects. The test subjects in previous research were male rats, whereas in this research

female rats were used. However, due to the design of the experimental setup, it is impossible to use male rats; their reproductive organs would hinder correct positioning inside the setup.

Furthermore, due to delays in the construction of the test setup, the rats used here were somewhat older than those reported in literature. However, while these differences might contribute somewhat to the observed differences, it is unlikely that they would explain a force which is only 30% of what would be expected, at a higher assumed indentation.

When looking at the MRI T_2 -weighted images of muscles which have been subjected to a mechanical load, we can see what looks like damage. It is evident only in the slices around the area where loading occurred. What is interesting is that the damage we see here is evident much sooner than expected; 30 minutes after unloading. However, previous research did not check for damage until 24h after unloading. It is not unlikely that, if an MRI scan had been made within 30 minutes of unloading, some evidence of damage would have been found there as well. Figures 5.3a-b show the cross-section of the leg at the location of the indenter, figure 5.3c shows the same from previous work. The muscle in (a) was loaded with approximately 0.5N during 2 hours, the scan shown here was taken approximately 30 minutes after load removal. Due to some technical difficulties, we unfortunately do not have a $t=0$ scan of the muscle, nor a 24h follow-up. The muscle in (b) was used for force measurements. The damage visible here resulted from multiple load applications, or impacts. It is much less clearly defined than in the muscle loaded for a full 2 hours, and after 18 hours, all traces seemed to have disappeared.

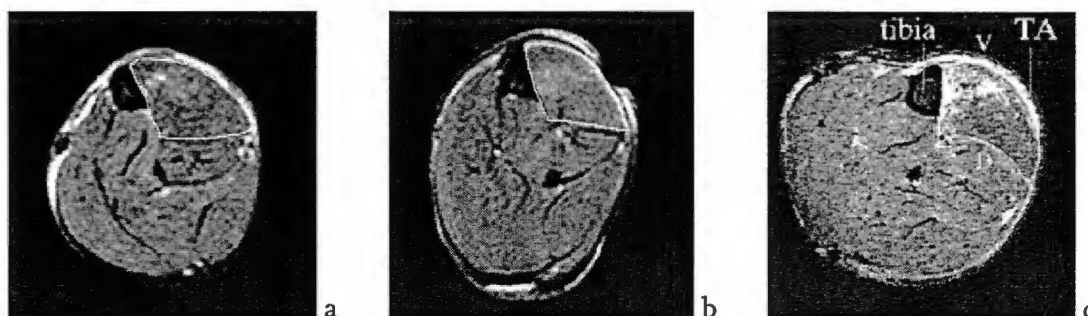


Figure 5.3: cross-sections of the muscle at location of the indenter. 4mm indentation, 0.5N load over a period of 2h, image taken 30minutes after unloading (a). 2.75mm indentation, 5 subsequent impact loadings starting at 0.6N and dropping to 0.45N, total load time perhaps 30 minutes, image taken 15 minutes after unloading (b). Reference image, unknown indentation, sustained load of 250kPa over 2 hours, image taken 24h after unloading [05] (c)

Using the modified FEM model, a reasonably accurate fit of the experimental data was accomplished (see figure 4.5).

However, since all loading was done at 2.75mm indentation depth, there was no way to determine the non-linearity in the Ogden model. Any imaginable combination of the parameters μ and α could yield the desired results (see figure 5.4). For this reason the exponent (α) was chosen as the lowest value reported in literature and only the modulus (μ) was used in the estimation process, as previously mentioned in section 4.3.

Depending on the severity of the problem with the Ogden model described in section 4.3, the values obtained here may need to be reassessed. For now, while parameters found in the current work will not have their definitive values, they provide an adequate fit to the experimentally obtained data, and may prove a good starting point for further study.

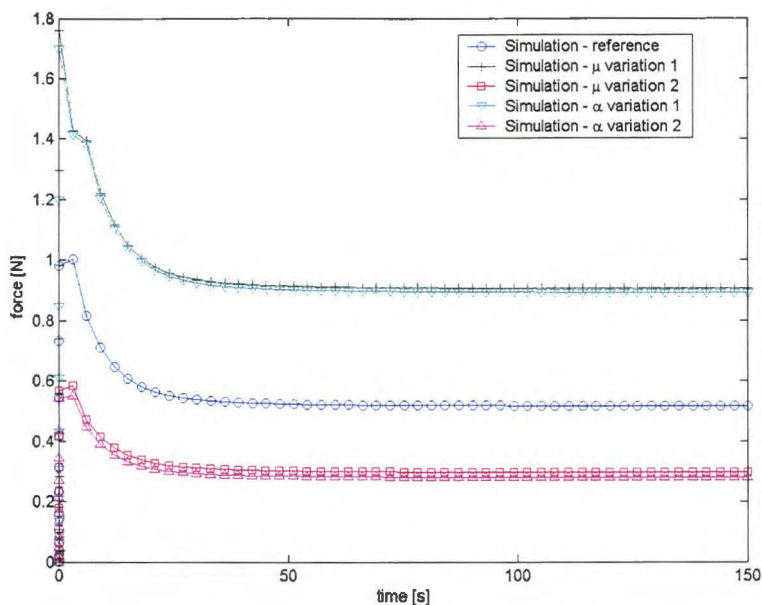


Figure 5.4: example of the influence both the μ and α parameters have on the results of the simulation. The middle line is the reference situation, above and below that are two superimposed lines, one was reached by varying μ , the other by varying α . All other parameters were kept at reference values.

As mentioned in section 3.2.2, the skin was attached to the muscle instead of being able to move freely across it. This resulted in a slight difference in the stress and strain distributions along the muscle-skin interface; the difference lies mainly in the distribution, the magnitude was similar in both cases.

Another point to consider, with respect to the model: the dorsal edge of the muscle can move unobstructed (figure 4.6), while in reality neighboring muscles would prevent, or hinder, this movement. The exact influence is not known, but if displacements along the dorsal edge were prevented, the muscle would offer greater resistance to deformation, suggesting that the stiffness would need to be lower to maintain the same reaction forces at this level of indentation.

What is also apparent from the comparison in figure 4.6 is that the indenter angle relative to the muscle differs from experiment to simulation. This is likely caused by the angle of the leg inside the cast, since the indenter angle is normally around 45 degrees relative to the RF coil and field of view on the MR scans.

The optimal position of the leg inside the plaster cast is when the ankle makes a 90 degree angle. This way the muscle is unloaded and will have the largest cross-section. It is, however, not always possible to ensure this angle. Either the leg shifts slightly during the application of plaster, or shortly after. It is also possible that, due to a poor view of the ankle itself during fixating, the ankle isn't actually positioned at 90 degrees before application of plaster.

The differences between cross-sections of the different rats are due to normal variability in the population, or due to the difference in sex when comparing to images from the previous study. However, some care must be taken when positioning the plastic braces in the cast, since carelessness might cause deformation of the leg.

As mentioned in the previous study [05]; although damage determined experimentally with the aid of MRI shows some overlap with the calculated shear distributions (figure 4.7), the result is not yet convincing enough to attribute muscle damage to cell deformation. The tagging experiments described in section 3.1.1 might improve our understanding of the mechanics of muscle deformation. Strain fields obtained in this fashion could be matched to strain fields resulting from simulations. It is obvious that this requires further research.

Finally, as the ultimate goal of the project this research is part of, is to obtain parameters for use in the modeling of car crashes, one might wonder if the fact that the test subject is sedated during testing influences the results in any way. During an actual crash, the subject will be conscious, at least initially; muscles may not necessarily be as relaxed as they are in a sedated individual.

In conclusion: the methods described here seem promising in determining the mechanical properties of the muscle tissue. Once operational, tagging measurements will provide strain fields and displacement data. Force measurement can already be done accurately, both within and without the MR environment, and the apparatus is suited to providing a prolonged loading for damage assessment. Coupled with finite element simulations, the data obtained will yield a further improvement of the material parameters reported previously.

6. Recommendations

In future work, experiments should be done on a larger population of animals, to obtain a larger spread of force responses, both at the current indentation level, and at higher levels. Data from these experiments will help to further improve the material parameters.

Further damage evolution experiments need to be done, taking care to take initial ($t=0$) scans as reference. Furthermore, for these experiments a greater indentation is needed than can be currently applied. Current indentation and resulting forces are too low to lead to lasting tissue damage.

Future experiments should be separated into force measurement experiments, MR Tagging experiments and damage evolution experiments. The reasons for this have been mentioned in the foregoing sections; if a set of force measurements, or a Tagging experiment, is combined with a damage evolution experiment, it is not possible to determine whether resulting damage, if present, is due to impact loading, prolonged loading, or both.

With respects to preparation for the experiments, care must be taken to position the ankle at 90° , but also that the tibia and fibula are aligned vertically. That way the location and angle of the indenter will correspond better to those of the simulation. If this is difficult to implement, perhaps the model should be modified to closer resemble reality.

Another possible improvement of the finite element model would be to model the entire cross-section of the leg, as the free displacements along the dorsal edge are not physiologically realistic.

Acknowledgements

I would like to thank everyone who helped me over the course of this project; Cees Oomens, for steering me in the right direction when necessary, and for his help with the numerical aspects of this project. Anke Stekelenburg for getting me started, and providing me with useful information when/if needed. Rob v/d Berg for his part in the construction of the set-up. I would like to thank Larry de Graaf both for his help with ideas for the design of the indenter unit, and the construction and servicing of the MR part of the experimental set-up. Rob Petterson for helping with strain gage selection and signal measurement. Jo Habets for his help and instructions regarding work with laboratory animals. Piet Schreurs for answering my questions about the workings of the MSC.Marc software package. Gustav Strijkers for his help during the MRI experiments, general background information and also suggestions for the indenter unit. I would also like to thank Martijn Cox for his suggestions and help.

References

- [01] **Axel L., Dougherty L.**, (1989), "MR imaging of motion with spatial modulation of magnetization", *Radiology* 171, 841-845
- [02] **Axel L.**, (2002), "Biomechanical Dynamics of the Heart with MRI", *Annu. Rev. Biomed. Eng.* 2002, 4:321-347
- [03] **Basel M., Drost M.R., Wielders J.D.L., Huyghe J.M., Huson A., Janssen J.D.**, (1996), "Strain Distribution on Rat Medial Gastrocnemius (MG) During Passive Stretch", *J. Biomech* 1996. Vol. 29 No.8, p. 1069-1074
- [04] **Basford J.R., Jenkyn T.R., An K.N., Ehman R.L., Heers G., Kaufman K.R.**, "Evaluation of healthy and diseased muscle with Magnetic Resonance Elastography", *Arch. Phys. Med. Rehabil.* Vol. 83, nov 2002
- [05] **Bosboom M.**, (2002), "Deformation as a trigger for pressure sore related muscle damage", Technische Universiteit Eindhoven, PhD Thesis
- [06] **Bosboom M., Oomens C.W.J., Bouten C.V.C., Drost M.R., Baaijens F.P.T.**, (2001), "Passive transverse mechanical properties of skeletal muscle under in vivo compression", *J. Biomech.* 34: p 1365-1368
- [07] **Bouten C.V.C., Cleutjens J.**, (2002), "Schade en Herstel (8W070)", Technische Universiteit Eindhoven, Lecture Notes
- [08] **Braakman N.**, (2003), "Determination of the Passive Transverse mechanical Properties of Skeletal Muscle under In Vivo Compression; Experimental and Numerical Aspects - A Literature Review", Technische Universiteit Eindhoven Internal Report, BMTE03.13
- [09] **Dai G., Gertler J.P., Kamm R.D.**, (1999), "The Effects of External Compression on Venous Blood Flow and Tissue Deformation in the Lower Leg", *J. Biomech Eng.* Dec 1999, vol. 121/557
- [10] **Dam E.A. van.**, (2003), "Functionality of Aortic Valves Inside a Bioreactor: Monitoring of Flow Patterns with MRI", Technische Universiteit Eindhoven Internal Report, BMTE03.05
- [11] **Den Camp O.M.G.C., Oomens C.W.J., Veldpaus F.E., Janssen J.D.**, (1991), "An efficient algorithm to estimate material parameters of biphasic mixtures", *Int. J. Numer. Meth. Eng.* 45, 1315-1331
- [12] **Dresner M.A., Rose G.H., Rossman P.J., Muthupillai R., Manduca A., Ehman R.L.**, (2001), "Magnetic Resonance Elastography of Skeletal Muscle", *JMRI* 13:269-276
- [13] **El-Khoury G.**, (2003), "Muscle Tear (Strain)", The University of Iowa, <http://www.vh.org/adult/provider/radiology/MuscleInjuries/07MuscleTearStrain.html>
- [14] **Fletcher, D.**, (1999), "MRI PHYSICS: A Nuts and Bolts Approach", <http://rad.usuhs.mil/rad/handouts/fletcher/fletcher/>
- [15] **Fung. Y.C.**, (1993), "Biomechanics - Mechanical Properties of Living Tissues", 2nd Edition, Springer-Verlag New York
- [16] **Gelb A. (ed.)**, (1999), "Applied Optimal Estimation", 15th printing, © 1974 The Analyst Sciences Corporation
- [17] **Gielen A.W.J.**, (1998), "A continuum approach to the mechanics of contracting skeletal muscle", Technische Universiteit Eindhoven, PhD Thesis; WenST Library: PFN 98 GIE
- [18] **Haber I, Metaxas D.N., Axel L.**, (2000), "Three dimensional motion reconstruction and analysis of the right ventricle using tagged MRI", *Medical Image Analysis* 4, p. 335-355
- [19] **Hargen A.R., Schmid-Schönbein G.W.**, (2003), "Mechanics of Tissue and Lymphatic Transport", Chpt. 17 from "Biomechanics - Principles and Applications" © CRC Press LLC
- [20] **Heers G., Jenkyn T.R., Klein M.O., Kaufman K.R., Ehman R.L., An K.N.**, (2001), "Magnetic Resonance Elastography; a non-invasive method to determine muscle activity in vivo". Mayo clinic - Orthopedic Mech. Lab, Magn. Resonance Lab. contact: an.kainan@mayo.edu

- [21] **Hendriks M.**, (1991), "*Identification of the Mechanical Behavior of Solid Materials*", Technische Universiteit Eindhoven, PhD Thesis
- [22] **Hornak J.P.**, (2003), "*The Basics of MRI*"; <http://www.cis.rit.edu/htbooks/mri/index.html>
- [23] **Jenkyn T.R., Ehman R.L., An K.N.**, (2003), "*Noninvasive muscle tension measurement using the novel technique of Magnetic Resonance Elastography (MRE)*", Short Communication, J. Biomech. MS#2001-169 - (to be published)
- [24] **Jones D.A., Round J.M.**, (1996), "*Skeletal Muscle in Health and Disease - A Textbook of Muscle Physiology*", Manchester University Press
- [25] **Maenhout M.**, (2002), "*Strain fields within contracting skeletal muscle*", Technische Universiteit Eindhoven, PhD Thesis
- [26] **Martins J.A.C., Pires E.B., Salgado R., Dinis P.B.**, (1998), "*A Numerical model of passive and active behavior of skeletal muscles*", *Compu. Methods Appl. Mech. Engrg.* 151: 419-423
- [27] **Meeuwissen M.H.H., Oomens C.W.J., Baaijens F.P.T., Petterson R., Janssen J.D.**, (1998), "*Determination of the elasto-plastic properties of aluminium using a mixed numerical-experimental method*", *Journal of Materials Processing Technology* 75 p. 204-211 (see also Meeuwissen PhD thesis)
- [28] **Meeuwissen M.H.H.**, (1998), "*An Inverse Method for the Mechanical Characterisation of Metals*", Technische Universiteit Eindhoven, PhD Thesis
- [29] **Moore C.C.**, (2000), "*Three-dimensional Systolic Strain Patterns in the Normal Human Left Ventricle: Characterization with Tagged MR Imaging*", *Radiology* 2000, 214:453-466
- [30] **Moser K.W., Georgiadis J.G., Buckius R.O.**, (2001), "*On the use of optical flow methods with spin-tagging MRI*", *Annals of Biomedical Engineering*, vol. 29 pp. 9-17
- [31] **MSC.Software Corporation**, (2000), "*MSC.Marc Volume A: Theory and User Information, Version 2000*", Copyright © 2000 MSC.Software Corporation.
- [32] **MSC.Software Corporation**, (2000), "*MSC.Marc Volume C: Program Input, Version 2000*", Copyright © 2000 MSC.Software Corporation.
- [33] **Nagel E., Fleck E.**, (2001), "*Magnetic Resonance Imaging (MRI) in cardiac diagnostics*", *Medica mundi* 45/1, p 23-30. (Reprinted from HeartCare)
- [34] **NessAiver M.**, (1997), "*All you really need to know about MRI physics*", University of Maryland Medical Center
- [35] **Ogden R.W.**, (1984), "*Non-Linear Elastic Deformations*", Ellis Horwood Limited, Chichester
- [36] **Oomens C.W.J., Bouten C.V.C.**, (2002), "*Mechanical Properties of Living Tissues (4Q530)*", Technische Universiteit Eindhoven, Lecture notes: 4783
- [37] **Oomens C.W.J., Ratingen M.R. van, Janssen J.D., Kok J.J., Hendriks M.A.W.**, (1993), "*A numerical-experimental method for a mechanical characterization of biological materials*", *J. Biomechanics* Vol. 26, No. 4/5, pp 617-621
- [38] **Osman N.F., Sampath S., Atalar E., Prince J.L.**, (2001), "*Imaging Longitudinal Cardiac Strain on Short-axis images using strain encoded MRI*", *Magnetic Resonance in Medicine* 46: 324-334
- [39] **Pelc N.J., et al.**, (1991), "*Phase contrast cine magnetic resonance imaging*", *Magn. Reson. Q.* 7:229-254
- [40] **Ratingen, M. van**, (1994), "*Mechanical Identification of Inhomogeneous Solids - A Mixed Numerical Experimental Approach*", Technische Universiteit Eindhoven, PhD Thesis
- [41] **Simo J.C.**, (1987), "*On a Fully Three-Dimensional Finite-Strain Viscoelastic Damage Model: Formulation and Computational Aspects*", *Computer Methods in Applied Mechanics and Engineering* 60 p153-173
- [42] **Stekelenburg A.**, (2003), "*Compression Induced Tissue Damage; Animal Models*", From: "*Current and Future Perspectives in Pressure Ulcer Research*", Eds.: D.L. Bader, C.V.C. Bouten, C.W.J. Oomens (to be published)

- [43] **Strijkers G., Nicolay N.**, (2003), "*Magnetic Resonance Imaging and Spectroscopy of Pressure Sores*", From: "Current and Future Perspectives in Pressure Ulcer Research", Eds.: D.L. Bader, C.V.C. Bouten, C.W.J. Oomens (to be published)
- [44] **Thomassen J.A.M.**, (1999), "*A numerical-experimental approach to determine the transverse mechanical properties of skeletal muscle*", Technische Universiteit Eindhoven, internal WFW-report 99.038
- [45] **Toorn A. van der, Barenburg P., Snoep G., Veen F.H. van der, Delhaas T., et al.**, (2002), "*Transmural gradients of cardiac myofiber shortening in aortic valve stenosis patients using MRI tagging*", Am. J. Heart Circ. Physiol. 283: H1609-1615
- [46] **Ugural A.C., Fenster S.K.**, (1995), "*Advanced Strength and Applied Elasticity - 3rd Edition*", © by Prentice-Hall PTR, Upper Saddle River, New Jersey
- [47] **Vick III G.W., Chung T., Beerbaum P., Muthupillai R.**, (2002), "*Role of MR flow imaging in assessing congenital heart disease*", MedicaMundi 46/1 53-58
- [48] **Vishay Measurements Group, Inc.**, june 2000, "*Micro-Measurements Catalog 500 - Precision Strain Gages*"
- [49] **Vishay Measurements Group, Inc.**, "*Strain Measurements on Composite Materials*", p.10-15, Epsilonics, april-october 1984
- [50] **Vishay Measurements Group, Inc.**, (2003), "*Protective Coatings - General information*", document number 11025, <http://www.vishaymg.com>
- [51] **Weaver J., Cheung Y., Hood M., Doyley M., Van Houten E., Kennedy F., Qin X., Paulsen K.**, (2002), "*MR Elastography of the weight bearing tissues of the foot developed in the effort to reduce diabetic foot amputations*"
Lay Language version of paper MO-D-518-7
AAPM/COMP/CCPM Meeting, Montréal, Quebec. July 2002

- [52] "*MRI: How It Works*"
<http://www.gcmradiology.com/mrworks.html>

- [53] "*MRI Q&A for Physicists: MR Contrast and Image Acquisition*"
<http://www.medphysics.leeds.ac.uk/~dmh/mri/questions/acquiringimages>

Appendix A MRI basics

Protons possess an intrinsic magnetic moment, called spin. When this magnetic moment is placed in a large external field, B_0 , it will precess around the axis of the external field (figure A.1.a). The frequency of this precession is proportional to the external field, according to

$$\omega_0 = \gamma B_0 \tag{A.1}$$

With ω_0 the frequency of precession or Larmor frequency, and γ the gyromagnetic ratio ($\gamma = 2\pi \cdot 42.56$ Mrad/s/Tesla for protons). For a large number of protons, the net magnetization will be aligned along B_0 . If a second magnetic field, B_1 , is applied perpendicular to B_0 , the magnetization vector M_0 will tip towards the xy-plane. This excitation is shown in figure A.1.b. B_1 is released by applying a radio frequency (RF) pulse with the Larmor frequency.

The angle of rotation (θ), or flip angle, of M_0 around B_1 is defined as

$$\theta = \gamma \tau B_1 \tag{A.2}$$

with τ the time during which the field B_1 (RF pulse) is switched on. The frequently used names 90° and 180° pulses refer to the tip angle of the magnetization vector caused by these pulses.

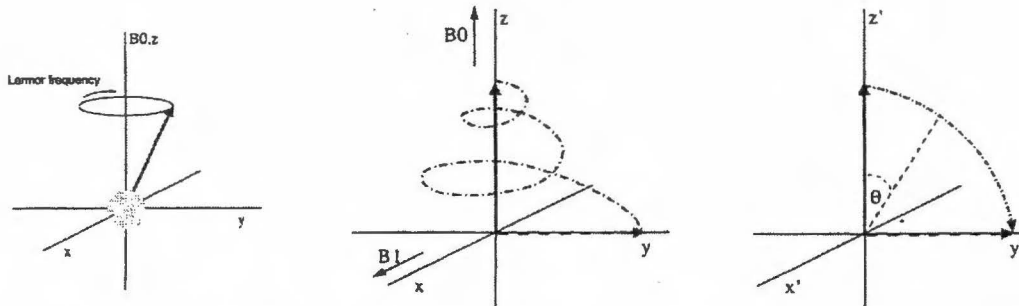


Figure A.1: Spinning proton (a), laboratory frame of reference (b), rotating frame of reference. Images reproduced from van Dam [10]

The coordinate system in figure A.1.b is referred to as the laboratory frame of reference. M_0 tips down toward the y-axis while it precesses around B_0 . To simplify the view on the magnetization vector, a coordinate system that precesses with the Larmor frequency is introduced: the rotating frame of reference (figure A.1.c). The precession of the magnetization vector in the xy-plane introduces an induction signal in the receiver coil. The length of the magnetization vector is the magnitude of the signal. The angle between the magnetization vector and the y-axis is referred to as the phase of the signal. A Free Induction Decay (FID) is the signal one acquires after applying only a 90° pulse. When no magnetic gradients influence the signal after a 90° pulse, a Free Induction Decay is the result. T_1 and T_2^* relaxation cause the signal to decay over time [10].

Time to Repetition (TR):

The TR is the amount of time between consecutive phase-encoding steps.

Time to Echo (TE):

TE is the time between the initial perturbing RF pulse and the center of the acquisition period. TR is generally longer than TE, except for some steady state fast scan methods.

T₁ relaxation time:

T₁ is the time constant characterizing the rate at which excited nuclei dissipate excess energy to the environment (lattice). It is referred to as the spin-lattice or longitudinal relaxation time.

T₁ is the time it requires to restore 63% of the equilibrium population of magnetic moments aligned with the B₀ magnetic field following the excitation pulse. T₁ is an exponential time constant and not the time for full recovery [10], [14], [22].

$$M_z(t) = M_o(1 - e^{-\frac{t}{T_1}}) \tag{A.3}$$

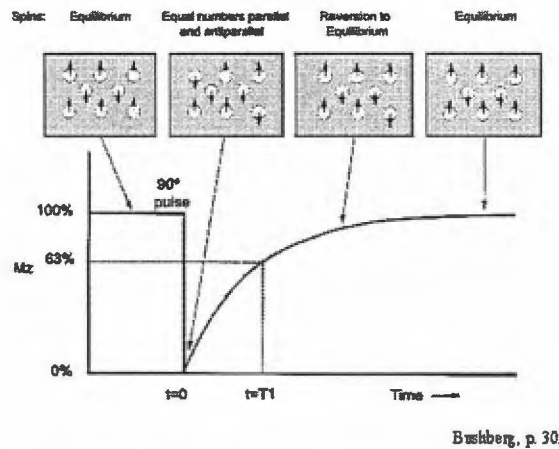


Figure A.2: T₁ relaxation time [14]

T₁ values range from 0.1 to 1 second in soft tissues and from 1 to 4 seconds in aqueous tissues and water. Because the number of spin-lattice interactions is dependent on the precessional frequency of protons, the T₁ relaxation time depends on the magnetic field strength.

T₂ relaxation time:

After excitation, the MR signal present in the xy-plane decays exponentially to zero over time. The time required for 63% of the signal to disappear irreversibly is called the T₂ relaxation time or the transverse or spin-spin relaxation time.

Mathematically, this exponential relationship can be expressed as:

$$M_{xy} = M_o e^{-\frac{t}{T_2}} \tag{A.4}$$

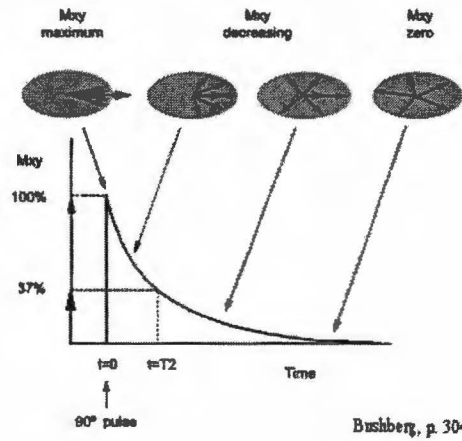


Figure A.3: T_2 relaxation time [14]

The T_2 relaxation time depends primarily on spin-spin interactions, which are non-reversible: we have no control over them. T_2^* depends on both spin-spin interactions and the homogeneity of the external magnetic field. It is, therefore, reversible. Homogeneity depends on how good your magnet is, as well as susceptibility-induced field distortions due to the presence of tissues or other objects in the field. T_2^* can be considered as the observed or effective transverse relaxation time. T_2^* is always less than T_2 . The two are related by the following equation [53]:

$$\frac{1}{T_2^*} = \frac{1}{T_2} + \gamma\Delta B \tag{A.5}$$

$\gamma\Delta B$ represents the relaxation rate contribution attributable to field inhomogeneities.

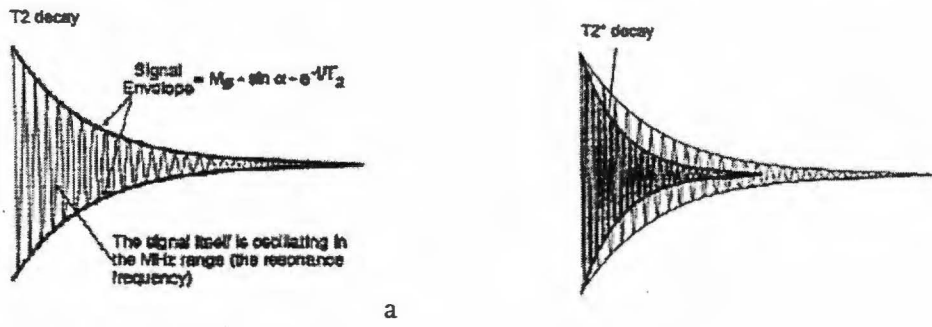


Figure A.4: T_2 (a) versus T_2^* (b) decay

T_2 and T_1 mechanisms are related to the rotational and tumbling frequency of molecules. Small molecules reorient more rapidly than larger molecules. The quicker a molecule reorients, the less dephasing is caused by adjacent protons.

Small molecules (e.g. liquids) exhibit shorter T_1 and longer T_2 . Larger molecules (e.g. lipids) tend to have longer T_1 and shorter T_2 .

In pure water T_2 and T_1 times are approximately identical. For biological material, the T_2 time is considerably shorter than the T_1 time.

T_1 weighted image:

The T_1 relaxation times for water and fat in the body range from 100 to 2000ms. The primary source of signal attenuation in a spin-echo image is the progressive saturation of the magnetic moment by the repetitive slice selection pulses. The signal from fat is bright, whereas image intensities from areas of muscle and fluid are lower. Cartilage, ligaments and tendons appear very dark. Bone marrow is also bright due to its fat content.

T_2 weighted image:

The exponential signal decay due to T_2 relaxation attenuates the signal from fluid and edema more slowly than the signal from fat, muscle, or normal connective tissues. Therefore, fluid and edema appear bright on T_2 -weighted MR. The fat displays moderate intensity whereas the muscles are hypointense. Tendons, ligaments and cartilage still appear dark. T_2 weighted images provide excellent contrast between normal and abnormal tissues. T_2 is related to the coherence of an ensemble of protons, and is a measure of the local molecular mobility. Increased water mobility (for example due to muscle damage) leads to increased T_2 relaxation time [52].

Compared to other soft tissues, normal skeletal muscle has an intermediate to slightly long T_1 relaxation time and short T_2 relaxation time. Muscle appears relatively hypointense on both T_1 - and T_2 - weighted sequences. The fat along fascial and subcutaneous tissue planes allows identification of individual muscles. All acute muscle injuries have associated edema and hemorrhage which cause prolongation of the T_1 and T_2 relaxation times of the injured tissue. Occasionally an added sequence utilizing fat suppression may be required. The bright signal from high water content stands out against the relatively low signal of muscle and intermediate signal of fat on T_2 -weighted images. T_1 -weighted images are less sensitive in depicting soft tissue abnormalities because most pathologic processes have long T_1 -relaxation times similar to muscle; the contrast between muscle and hemorrhage or between muscle and edema may be imperceptible on T_1 -weighted images [13]. The images in figure A.5 show the differences in T_1 - and T_2 -weighted images.

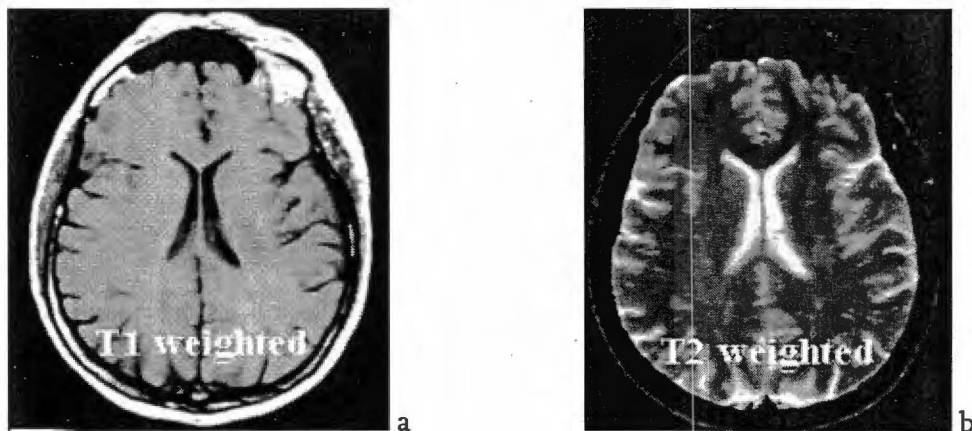


Figure A.5: Comparison of T_1 - (a) and T_2 -weighted (b) MR images of the brain. [52].

Appendix B MRI Slice Orientations

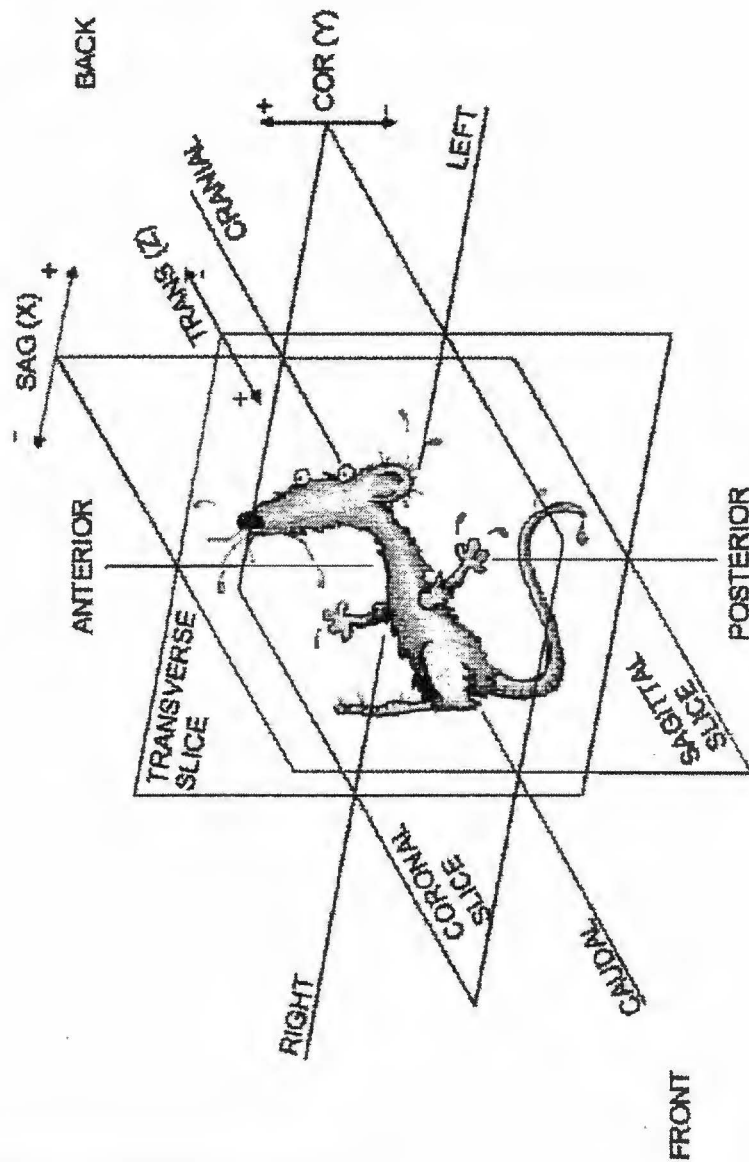
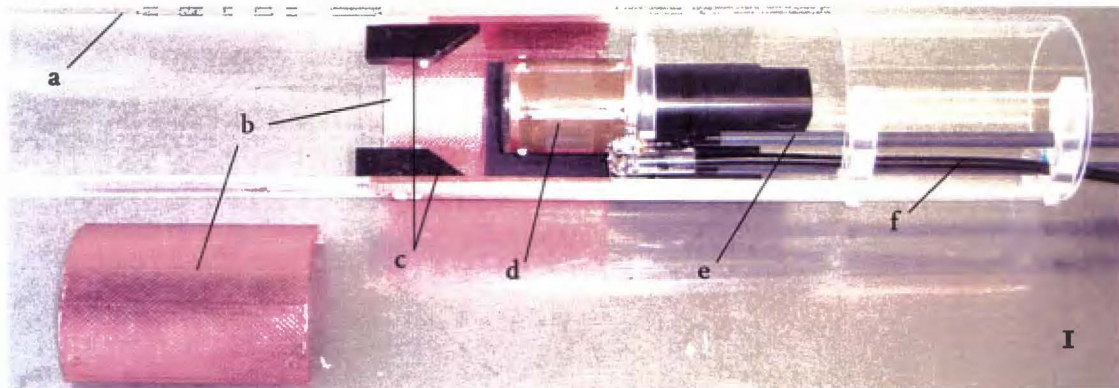


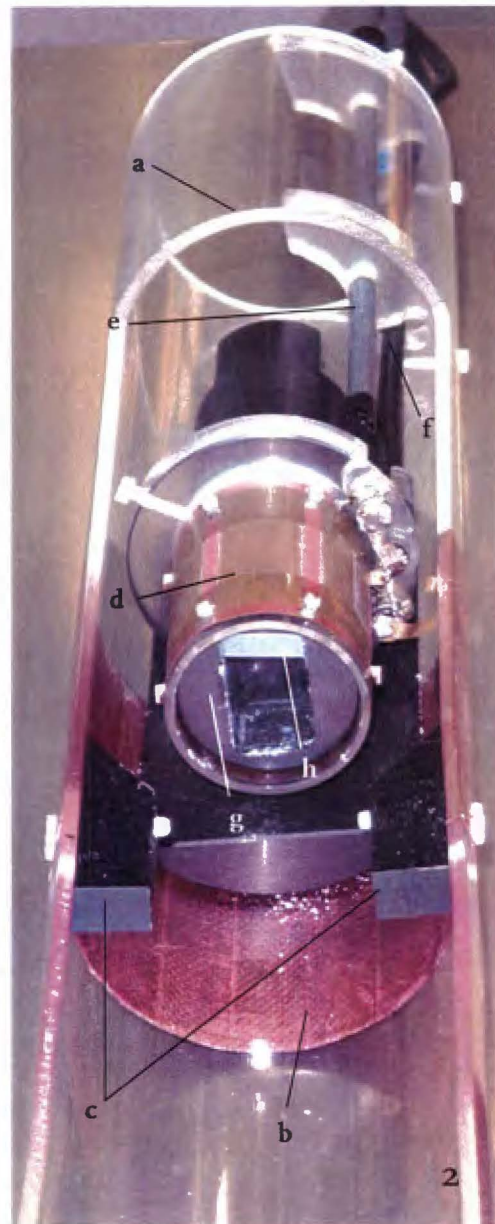
Figure A.1: explanation of the MRI slice orientations

Appendix C Overview of the Experimental Set-up



Experimental set-up (1-4):

- a inner housing
- b RF shield
- c clamps – to fixate the leg / plaster
- d RF coil
- e tune stick
- f sensor cable – carries signal from the coil to the computer
- g inner clamp – to ensure optimal positioning of the leg within the coil.
- h clip – to hold the leg / plaster securely in the inner clamp
- i hole cut into the RF coil to accommodate the indenter
- j outer housing which holds the inner housing and indenter unit once inside the MR environment.
- k indenter unit fixed to the outer housing



Appendix D Indenter Unit Design

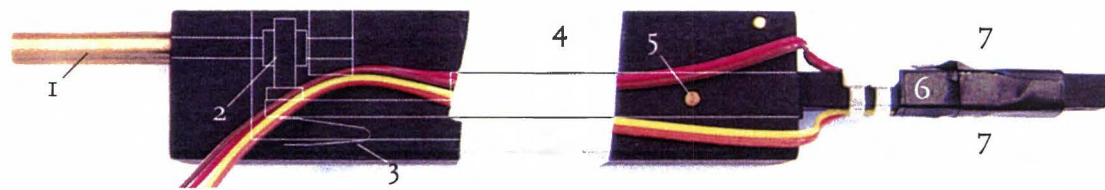


Figure D.1: The components of the indenter unit (a, b) – drive shaft (1), cam (2), spring (3), housing (4), hinge point (5), loading beam (6) with strain gages (7)

The dimensions of the indenter unit components are shown in the following figures. The housing and bending beam are made of Ertalon 66 GF30, a glass fiber filled polymer of the Nylon family (Appendix E). Other materials used are brass (drive shaft, cam, hinge point) and copper (spring).

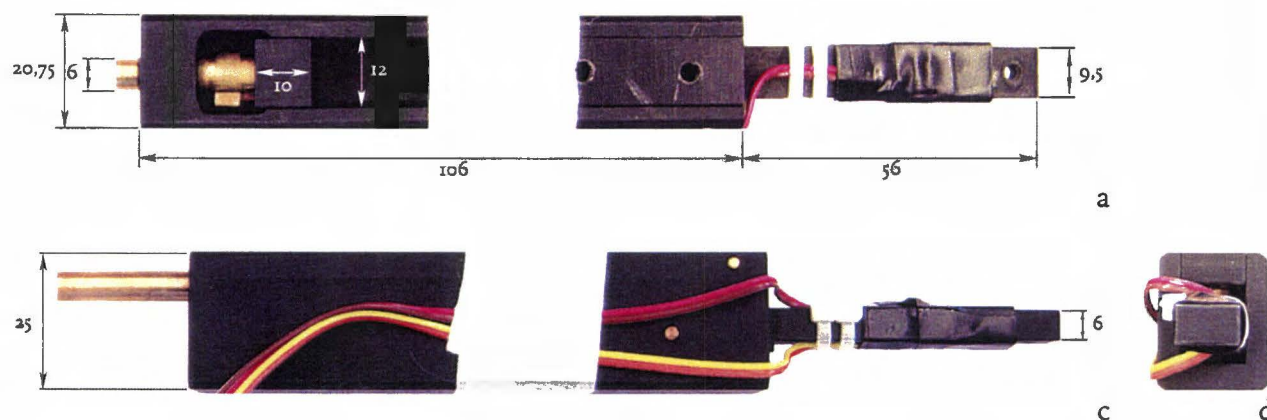


Figure D.2: Dimensioning of the indenter unit: top view (a), rear view (b), side view (c), frontal view (d)

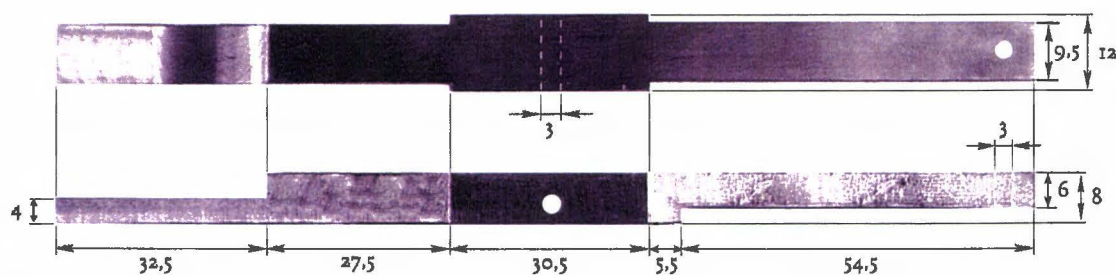


Figure D.3: Dimensioning of the indenter unit; indenter arm, top and side views

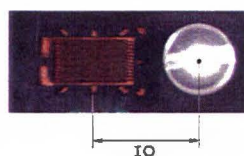


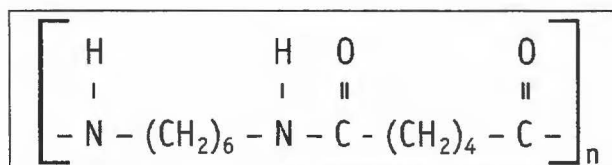
Figure D.4: Location of the strain gages relative to the indenter pin

Appendix E Product Data Sheet - Ertalon 66 GF30

Compared with virgin material this 30% glass fiber reinforced nylon grade offers increased strength, stiffness, creep resistance and dimensional stability whilst retaining an excellent wear resistance. It also allows higher maximum service temperatures. The tensile modulus is many times higher than that of the non-reinforced variant.

Key Features and Benefits:

- High mechanical strength
- Good fatigue resistance
- High mechanical damping ability
- Good sliding properties
- Excellent wear resistance



Physical Properties (indicative values)

Properties	ASTM Test Method	Units	Values
Color	-	-	Black
Specific Gravity	D792	-	1.29
Water Absorption:			
- at saturation in air of 23°C/50% RH	D570	%	1.7
- at saturation in water of 23°C	D570	%	5.5
Mechanical Properties:			
Tensile Strength	D638	N/mm ²	140 - 190
Tensile Modulus	D638	N/mm ²	7500 - 10000
Elongation	D638	%	3 - 5
Flexural Strength	D790	N/mm ²	200
Flexural Modulus	D790	N/mm ²	-
Hardness	Shore D	-	98
Thermal Properties:			
Melt Point	D2117	°C	255
Max allowable service temp in air			
- for short periods (1)	-	°C	250
- continuously for 20000hrs (2)	-	°C	110
Minimum Service Temperature	-	°C	-20
Linear thermal expansion coefficient	D696	m/m.K	4.5 - 5.5 x 10 ⁻⁵
Thermal Conductivity	C117	W/K.m	0.24
Flammability	D635	-	Self Extinguishing
UL (thickness in mm)	UL-94	-	HB
[Tests carried out using UL test methods by DSM EPP]			
Electrical properties			
Volume Resistivity	D257	Ω.cm	10 ¹⁴ - 10 ¹⁵
Dielectric Strength (3)	D149	kV/mm	20 - 30
Outside applications - UV resistance	-	-	A
Acids - Strong [pH < 3]	-	-	C
Alkalis - Strong [pH > 11]	-	-	A
Chlorinated Hydrocarbons	-	-	B
Hot Water	-	-	B

- (1) Only a few hours, with little or no load applied
- (2) After these periods mechanical properties reduce by approx 50%. Note, however, that service temperatures are load and time dependant.
- (3) Test specimen 1.6mm thick unless otherwise stated.
- 'A' No attack
- 'B' Mild attack by absorption
- 'C' Dimensional change due to absorption
- 'D' Decomposition in short time
- 'E' In steam - at 160°C, decomposition after short time

The data are typical values and are not intended to represent specifications. Their aim is to guide the user towards a material choice. All statements, technical information and recommendations in this product data sheet are presented in good faith, based upon test believed to be reliable and practical field experience. However, Bay Plastics Ltd cannot guarantee the accuracy or completeness of this information, and, it is the customer's responsibility to determine the suitability of products in any given application.

Partner in kennis
<http://www.eriks.nl>

ERIKS

Ertalon® is a registered trade mark of ERTA N.V

Appendix F Cam Design

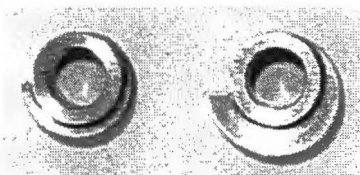
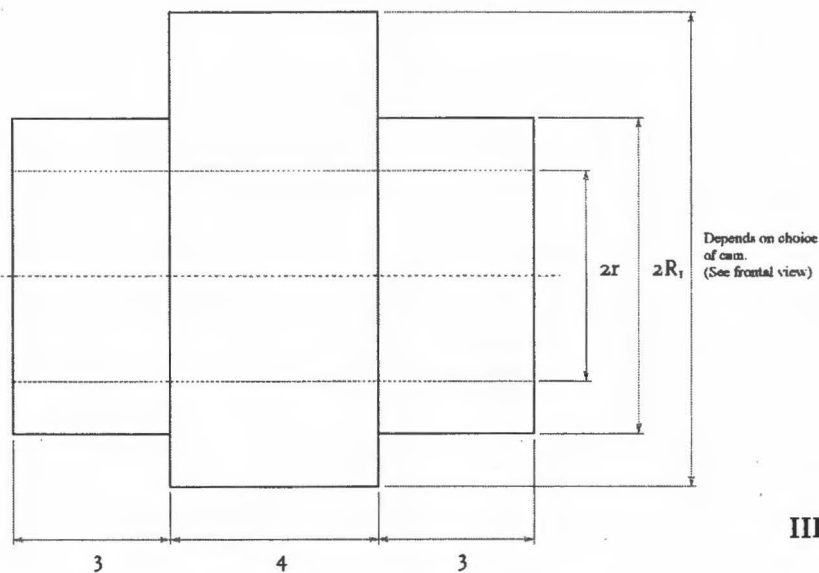
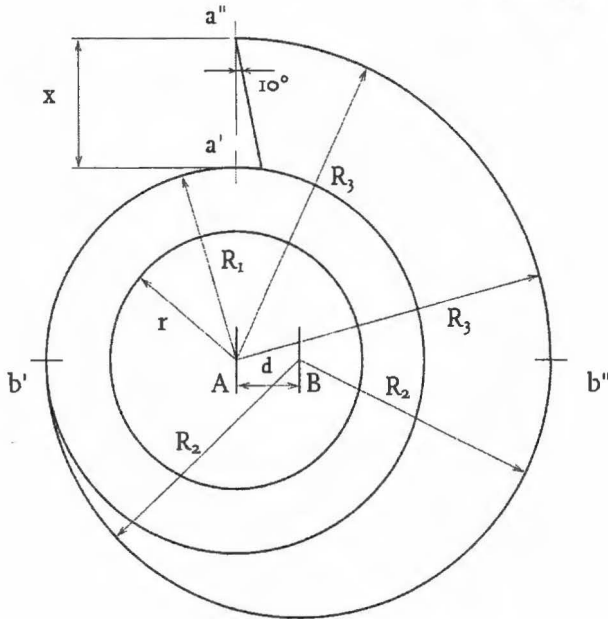
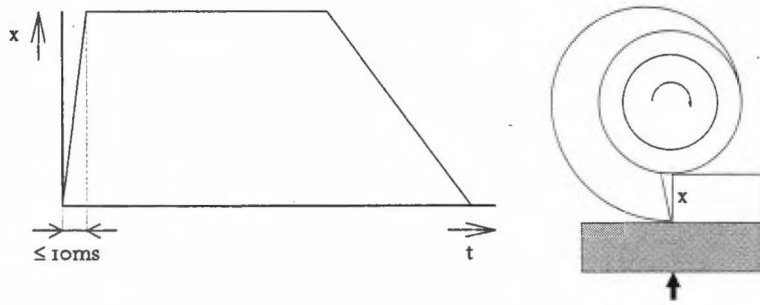


Figure F.1: General Cam design

dimensions in mm
material used: brass

I) Required displacement characteristic

II) Front view:

x : desired indentation depth
 r : radius of drive shaft = $2p6$
 R_1 : Base radius of the cam = 3
 R_3 : $R_1 + x$
 R_2 : $(R_1 + R_3)/2$

A: center (of rotation) of the cam and drive shaft

B: center of the transitional diameter running 180° from b' to b'' .

d : distance between A and B
 $= (R_2 - R_1)$

The 10° angle at point a'' is to make sure that, once this point is passed, the arm cannot get caught on the cam, but instantly displace over the desired distance x .

III) Side view:

$2r = 4p6$
 $2R_1 = 6$

Outer diameter is variable, and depends on the choice of the other parameters.

$p6$ is a measure of accuracy, here it ensures the cam has a tight fit around the drive shaft.

IV) Examples of two completed cams:

The left has an indentation (x) of 1mm, and the right 2mm.

Appendix G Indenter Unit: Maximum Strains

Before choosing a strain gage adequate for use in current experimental work, some calculations need to be done to determine the maximum strains that will be reached.

The problem is simply that of a bending beam [46].

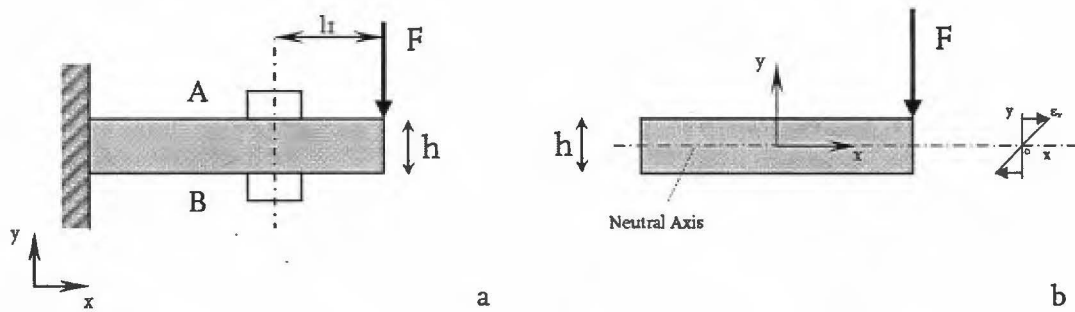


Figure G.1: Position of gages and dimensions of beam (a), explanation of neutral axis and strains (b)

$$\epsilon_x = \frac{M}{E \cdot W} = \frac{F \cdot l_i}{E \cdot W} \quad (\text{G.1})$$

ϵ_x	: strain in x-direction	[-]
M	: bending moment at local cross-section	[N·mm]
F	: load (to be measured)	[N]
E	: Elastic (Young's) modulus	[N/mm ²]
l_i	: position of strain gage relative to the point of force application	[mm]
h	: height of the beam	[mm]
W	: resistance moment of beam; $W = I/y$	[mm ³]
I	: moment of inertia; $I = 1/12 b \cdot h^3$	[mm ⁴]
y	: height measured from neutral axis (normally $1/2 \cdot h$)	[mm]
b	: width of beam	[mm]

Combining these we can write for ϵ_x :

$$\epsilon_x = \frac{12 \cdot F \cdot l_i \cdot y}{E \cdot b \cdot h^3} \quad (\text{G.2})$$

From the Ertalon Data sheet we find a Young's modulus of 7500 to 10000 N/mm², depending on humidity.

From previous experimental work [05] and early experiments, the maximum force is believed to lie in the 2-5 N range.

The dimensions of the bending arm used in the indenter unit are the maximum possible within the set-up while still maintaining functionality. The width and height of the beam are 9.5 and 6mm, respectively. The strain gage is attached with its center 10mm from the center of the indenter pin (see Appendix D).

Taking the highest expected force, and the lowest Young's modulus, we can calculate the highest expected strain:

$$\epsilon_x = \frac{12 \cdot F \cdot l_i \cdot y}{E \cdot b \cdot h^3}$$

With:

F = 5	[N]
E = 7500	[N/mm ²]
l _i = 10	[mm]
h = 6	[mm]
y = 3	[mm]
b = 9.5	[mm]

We find for the maximum strain $\epsilon_x = 1.17 \cdot 10^{-4}$

Appendix H Strain Gages

Gage Series	Description and Primary Application	Temperature Range	Strain Range	Fatigue Life	
				Strain Level in $\mu\epsilon$	No. of Cycles
CEA	Universal general-purpose strain gages. Constantan grid completely encapsulated in polyimide, with large, rugged copper-coated tabs. Primarily used for general purpose static and dynamic stress analysis.	Normal: -75°C to $+175^{\circ}\text{C}$	$\pm 3\%$ for gage lengths under 3.2mm $\pm 5\%$ for 3.2mm and over	± 1500 ± 1500	10^5 10^{6*}

Table H.1: General strain gage data [48]


250UW				'C' FEATURE		General-purpose gage. Exposed solder tab area 0.10 x 0.07 in (2.5 x 1.8 mm).	
							
GAGE LENGTH	OVERALL LENGTH	GRID WIDTH	OVERALL WIDTH			<p>CEA-Series Strain Gages feature large copper solder tabs and a completely encapsulated grid.</p> <p>Available with Option P2 (preattached leadwire cables).</p>	
				CEA-XX-250UW-120	120 $\pm 0.3\%$		
				CEA-XX-250UW-175	175 $\pm 0.3\%$		
				CEA-XX-250UW-350	350 $\pm 0.3\%$		
				CEA-XX-250UW-10C	1000 $\pm 0.3\%$		
Matrix Size (mm)			14.0L x 6.9W				

Table H.2: Strain Gage properties and dimensions [48]

Based on the data provided, the above strain gage was recommended by the supplier: The Vishay Measurements Group CEA-06-250UW-350 strain gage.

These strain gages are self temperature compensating. The 06 denotes the group with temperature compensation based on the expansion coefficient of steel.

Due to the fact that our set-up needs to be MR compatible, the indenter unit is made out of a polymer composite (Appendix E) instead of steel; Many composites are rather poor thermal conductors, so the gage resistance should be selected to minimize self heating effects. Higher resistance is preferable (350 ohm)

Temperature induced apparent strain (or apparent strain) is the name given to the false strain signal which occurs in a quarter bridge circuit whenever the initial bridge balance and subsequent strain measurement are performed at different temperatures. For metals most of the error is eliminated by using a self temperature compensated (S-T-C) gage.

When doing short duration tests, using a 1/2 or full bridge circuit, temperature compensation is not required, and the S-T-C number can be selected primarily on the basis of availability. An S-T-C number must still be specified for the gages; and it might as well be an intermediate one, corresponding to the widest selection and availability of stock. [48] [49]

The recommended adhesive (M-Bond AE-10) to attach the gages to the experimental setup, while generally used in combination with polymer composites, is incompatible with the material used here. An alternative was found in Loctite[®] Cyano-Acrylate glue.

Once installed, the gages have to be protected from damage. This damage can be caused by a range of factors: tension on the signal wires, humidity, fingerprints on the gage, and scratches on the surface of the gage.

To protect against damage caused by pulling on the signal wires, they were attached to terminals, which in turn were connected to the leads on the gages. Furthermore, the wires were fixated against the beam by means of tie-wraps (see figure H.1a).

To protect against humidity, fingerprints, and other contaminants, the gages and part of their surroundings were coated using M-Coat A, a polyurethane coating that can be 'painted' on (see figure H.1b). To protect against scratches and other physical damage, a collar of electrical tape was placed around the arm and gages (it is not actually stuck on the gages themselves), figure H.1c

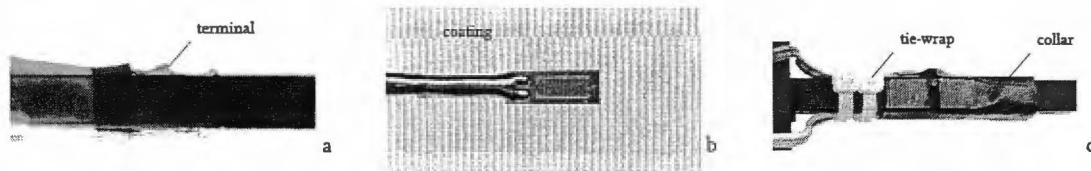


Figure H.1: Strain gage protection – terminals (a), coating [50] (b), tie-wraps & collar (c)

Appendix I Signal Measurement

Strain signals are measured using a Peekel carrier signal amplifier (pictured below). The unit consists of MCA130, CA100 and CCA100 components. The first is the base unit. With the CA100 the system's sensitivity can be adjusted and capacitive effects balanced out. Also, this unit is used to calibrate the strain measurements. The CCA100 component serves to zero the system by balancing the bridge resistances. The Amplifier can measure using either 1/2 or full Bridge of Wheatstone set-ups.



Figure I.1: Peekel Instruments Carrier Signal Amplifier with MCA130, CA100 and CCA100 components

As mentioned in the previous section, using a 1/2 or full Bridge of Wheatstone temperature effects can be minimized. This can be explained as follows (for a 1/2 Bridge circuit):

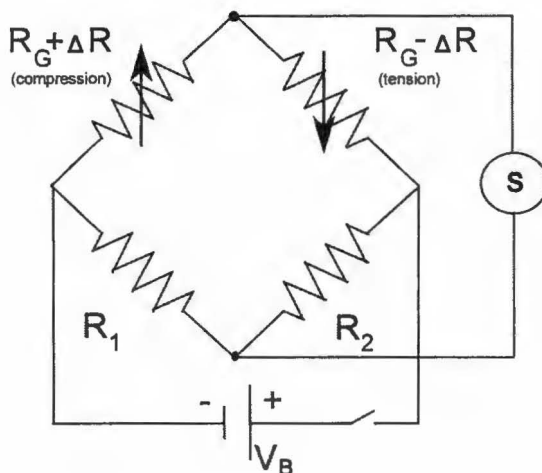


Figure I.2: Bridge of Wheatstone circuit with two strain gages (1/2 Bridge configuration)

The two strain gages are inserted into the circuit as pictured above. R_G is the base gage resistance; R_1 and R_2 are internal resistances of the signal amplifier. Their ratio can be modified on the CCA100 component of the signal amplifier.

The measured output voltage (S) is equal to:

$$S = \left[\frac{(R_G + \Delta R)}{(R_G + \Delta R) + (R_G - \Delta R)} - \frac{R_1}{R_1 + R_2} \right] \cdot V_B \quad (I.1)$$

When no load is applied, gage resistances are equal (R_G).

The bridge is said to be balanced when the output voltage S is zero. From the equation for S it is apparent that this is true when:

$$\frac{R_1}{R_2} = \frac{R_G + \Delta R}{R_G - \Delta R} \quad (I.2)$$

Or, in the unloaded situation, when $R_1/R_2 = 1$

Any changes in the strain gage resistance unbalance the bridge and produce a nonzero output voltage.

With all strain gages in a bridge at the same temperature and mounted on the same material, any changes in temperature affect all gages in the same way. Because the temperature changes are identical in the gages, the ratio of their resistance does not change, and the output voltage of the gage does not change:

$$\frac{R_1}{R_2} = \frac{R_G + R_T}{R_G + R_T} \quad (I.3)$$

Here R_T denotes the resistance change due to thermal expansion or shrinkage. Since both gage resistances change by equal amounts, the bridge balance is left intact.

Using a half bridge configuration is the simplest way to compensate for temperature drift.

Appendix J Strain Gage Calibration

Before calibration was done, the signal amplifier with indenter unit were switched on and left for approximately one hour to allow temperature effects (due to the heating of electrical components) to stabilize.

Once the system was stable, capacitive and resistive effects were zeroed.

A series of 7 known weights were used for calibration. Since early simulations predicted experimental forces in the order of 2N, calibration weights were selected in the range 50-225 grams (0.5-2.2 N)

For calibration a weight of 147 grams was used taken as reference weight; the amplification was adjusted so that once loaded with this weight the readout showed 147.

Once this was done subsequent weights were applied, and measured values were noted (table J.1). The true vs. measured values are shown in the calibration graph.

True value [g]	0	52	104	138	147	178	198	224
Measured value [g]	0	59	108	138	147	176	194	235

Table J.1: 1st series of calibration measurements

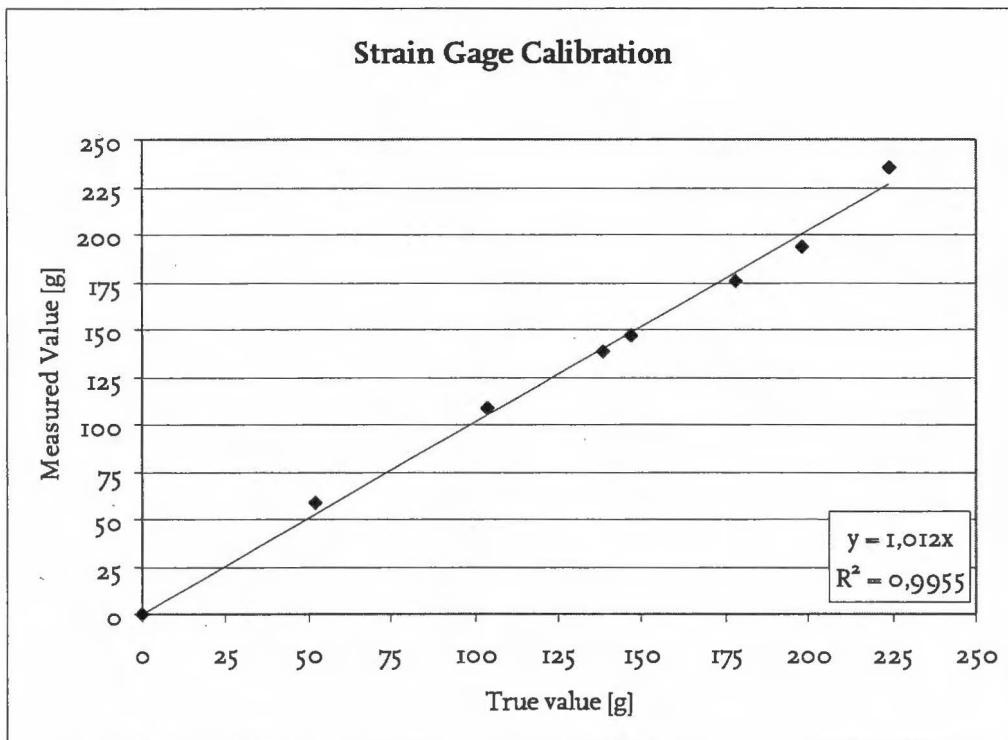


Figure J.1: 1st series of calibration measurements

The resulting calibration graph shows good linearity, with a high R^2 value. After the first actual experiments using laboratory animals, it became clear that experimental forces were lower than predicted by the model (in the order of 0.5-0.6N, or 50-60 grams).

To determine the accuracy of measurements in this range, a second calibration was done, using weights ranging from 16 – 178 grams.

In contrast to the previous calibration no reference weight was used, and the magnitude of amplification was not adjusted. The amplifier was zeroed and consequently the unmodified signal was noted for every weight (table J.2). Results are again plotted in a calibration graph.

Weight [g]	0	16	24	31	36	49	52	76	104	138	147	178
Force [N]	0	0.16	0.24	0.3	0.36	0.48	0.51	0.75	1.02	1.35	1.45	1.75
signal	0	0.045	0.065	0.082	0.096	0.127	0.136	0.195	0.262	0.341	0.355	0.443

Table J.2: 2nd series of calibration measurements, unmodified carrier signal

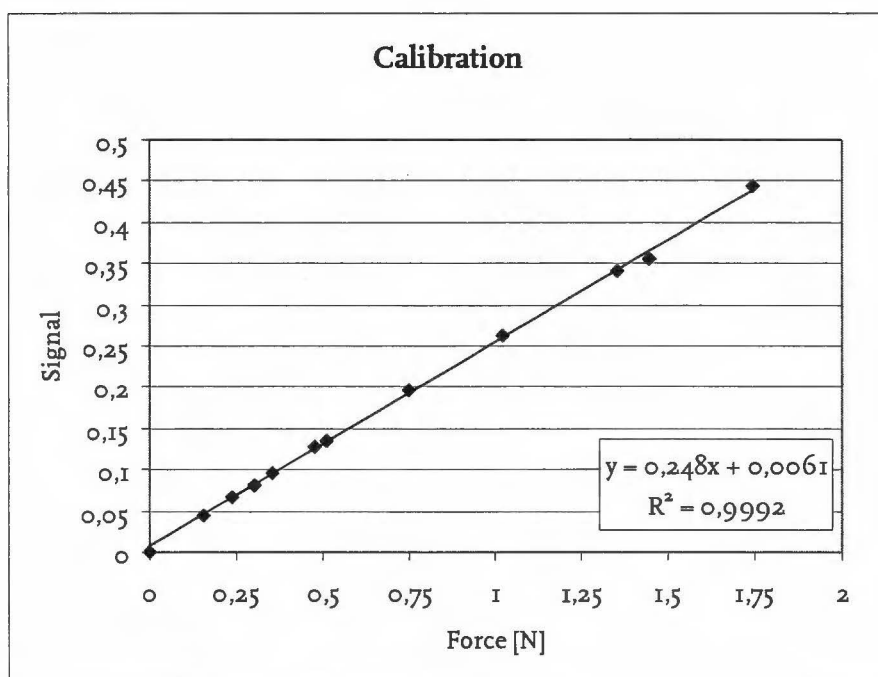


Figure J.2: 2nd series of calibration measurements.

From this graph it would seem that linearity is slightly better in the lower force ranges.

Appendix K Viscoelastic Ogden

As noted in section 4.3, the implementation of viscoelasticity in the Ogden model (equation 4.1) is incomplete; closer inspection of the equation will show that dimensions do not agree. The correct form is described below.

The correct stress relation, as described in the Marc manuals [32] [33], is given below. To avoid confusion further on, the Ogden parameter δ will be replaced here by θ .

$$\mathbf{S} = (1 - \theta) \frac{\partial \mathbf{W}}{\partial \mathbf{E}} + \int_{-\infty}^t \theta \frac{\partial \mathbf{W}}{\partial \mathbf{E}} G(t - \xi) d\xi \quad (\text{K.1})$$

The relaxation function $G(t)$ is given by:

$$G(t - \xi) = e^{-(t-\xi)/\tau} \quad (\text{K.2})$$

The strain energy function remains unchanged:

$$\mathbf{W} = \frac{\mu}{\alpha} (\lambda_1^\alpha + \lambda_2^\alpha + \lambda_3^\alpha - 3) \quad (\text{K.3})$$

If we look only at the first principal stress this yields

$$S_{11} = \frac{\partial \mathbf{W}}{\partial E_{11}} \quad (\text{K.4})$$

Due to the decoupling into 'extra' stress, indices will be dropped from here on.

Using the Green-Lagrange strain formulation, λ can be written as follows:

$$\lambda = (2e + 1)^{\frac{1}{2}} \quad (\text{K.5})$$

where e is the Green-Lagrange strain.

Differentiation of the strain energy with respect to the strain yields the following equation for the stress:

$$\mathbf{S} = \frac{d\mathbf{W}}{de} = \frac{\mu}{\alpha} \cdot \frac{1}{2} \cdot \alpha (2e + 1)^{\frac{1}{2}\alpha - 1} \cdot 2 = \mu (2e + 1)^{\frac{1}{2}\alpha - 1} \quad (\text{K.6})$$

For very small strains, this simplifies to:

$$\lim_{e \rightarrow 0} \mu (2e + 1)^{\frac{1}{2}\alpha - 1} = \mu \quad (\text{K.7})$$

The corrected viscoelastic form from equation 4.1 can be rewritten:

$$\frac{\dot{\partial W}}{\partial e} = \frac{\partial^2 W}{\partial e^2} \cdot \frac{\partial e}{\partial t} = \frac{\partial^2 W}{\partial e^2} \cdot \dot{\epsilon}(t) \quad (\text{K.8})$$

where

$$\frac{\partial^2 W}{\partial e^2} = (\frac{1}{2}\alpha - 1) \mu (2e + 1)^{\frac{1}{2}\alpha - 2} \cdot 2 = (\alpha - 2) \mu (2e + 1)^{\frac{1}{2}\alpha - 2} \quad (\text{K.9})$$

Again, for very small strains this simplifies to:

$$\lim_{\epsilon \rightarrow 0} (\alpha - 2) \mu (2e + 1)^{\frac{1}{2}\alpha - 2} = (\alpha - 2) \mu \quad (\text{K.10})$$

Now, the time-dependent part of the viscoelastic equation equals:

$$\int_{-\infty}^t \theta (\alpha - 2) \mu (2e + 1)^{\frac{1}{2}\alpha - 2} \cdot G(t - \xi) \cdot \dot{\epsilon}(\xi) d\xi \quad (\text{K.11})$$

When applying a step in the strain the following applies:

$$e(\xi) = H(\xi) \cdot \epsilon_0$$

$$\dot{\epsilon}(\xi) = \delta(\xi)$$

Entering this into equation K.11, the integral can then be written:

$$\theta (\alpha - 2) \mu G(t) \quad (\text{K.12})$$

with $G(0)=1$ for a step in stress this results in:

$$S(0) = (1 - \theta) \mu + \theta (\alpha - 2) \mu \quad (\text{K.13})$$

rewriting this we obtain

$$S(0) = [1 + (\alpha - 3) \theta] \mu \quad (\text{K.14})$$

This is quite different from the form described in section 4.3; there $S(0)$ equals only μ .

For $t \rightarrow \infty$ the stress is given by equation K.15, which is the same as the form described previously.

$$S(\infty) = (1 - \theta) \mu \quad (\text{K.15})$$

This gives a very different relation between stress at $t=0$ and $t=\infty$ than is evident from the results from the numerical analysis:

The relation between the stress level at $t=0$ and $t=\infty$, using the equations derived in this section yield the following:

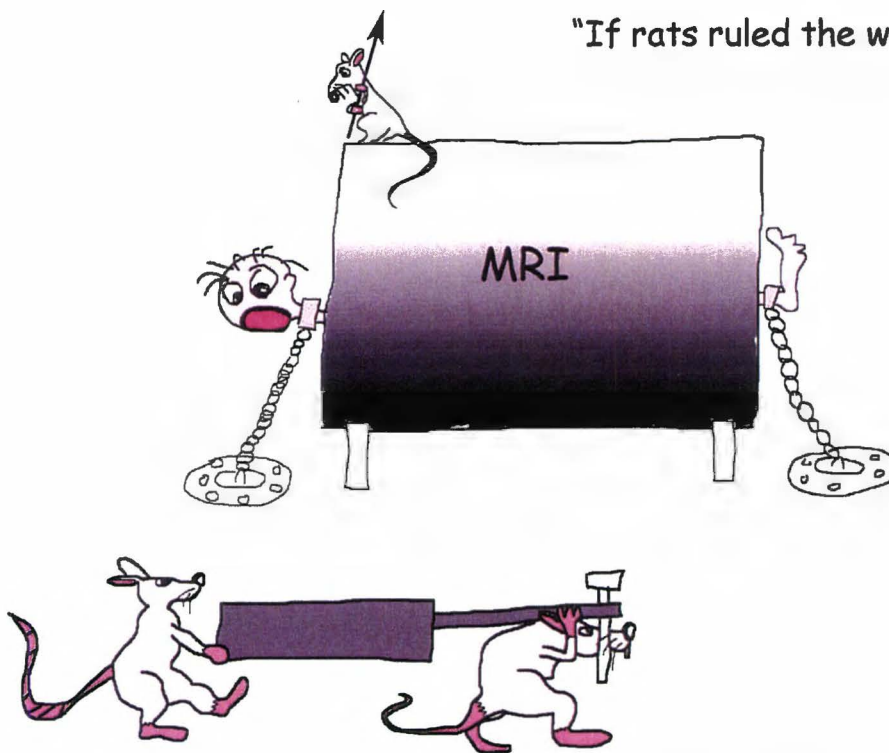
$$\frac{S(\infty)}{S(0)} = \frac{(1 - \theta)}{[1 + (\alpha - 3)\theta]} \quad (\text{K.16})$$

MSC.Marc, however, seems to behave according to formulation K.17:

$$\frac{S(\infty)}{S(0)} = (1 - \theta) \quad (\text{K.17})$$

credit: C.W.J. Oomens and M.A.J. Cox

"If rats ruled the world"



Niels Braakman, 2003